National Aeronautics and Space Administration

European Space Agency

Canadian Space Agency

Date: 2022 July 12

Characterization of JWST science performance from commissioning

Released

Jane Rigby[1], Marshall Perrin[2], Michael McElwain[1], Randy Kimble[1], Scott Friedman[2], Matt Lallo[2], René Doyon[3], Lee Feinberg[1], Pierre Ferruit[4], Alistair Glasse[5], Marcia Rieke[6], George Rieke[6], Gillian Wright[5], Chris Willott[7], Knicole Colon[1], Stefanie Milam[1], Susan Neff[1], Christopher Stark[1], Jeff Valenti[2], Jim Abell[1], Faith Abney[2], Yasin Abul-Huda[2], D. Scott Acton[8], Evan Adams[2], David Adler[2], Jonathan Aguilar[2], Nasif Ahmed[2], Loïc Albert[3], Stacey Alberts[6], David Aldridge[9], Marsha Allen[2], Martin Altenburg[10], Catarina Alves de Oliveira[4], Greg Anderson[1], Harry Anderson[2], Sara Anderson[2], Ioannis Argyriou[11], Amber Armstrong[2], Santiago Arribas[12], Etienne Artigau[3], Amanda Arvai[2], Charles Atkinson[13], Gregory Bacon[2], Thomas Bair[2], Kimberly Banks[1], Jaclyn Barrientes[2], Bruce Barringer[2], Peter Bartosik[9], William Bast[2], Pierre Baudoz[14], Thomas Beatty[6], Katie Bechtold[2], Tracy Beck[2], Eddie Bergeron[2], Matthew Bergkoetter[1], Rachana Bhatawdekar[4], Stephan Birkmann[4], Ronald Blazek[2], Claire Blome[2], Anthony Boccaletti[14], Torsten Boeker[4], John Boia[2], Nina Bonaventura[15], Nicholas Bond[1], Kari Bosley[2], Ray Boucarut[1], Matthew Bourque[2], Jeroen Bouwman[16], Gary Bower[2], Charles Bowers[1], Martha Boyer[2], Greg Brady[2], Hannah Braun[2], David Breda[17], Pamela Bresnahan[2], Stacey Bright[2], Christopher Britt[2], Asa Bromenschenkel[2], Brian Brooks[2], Keira Brooks[2], Bob Brown[8], Matthew Brown[2], Patricia Brown[2], Andy Bunker[18], Matthew Burger[2], Howard Bushouse[2], Steven Cale[1], Alex Cameron[18], Peter Cameron[9], Alicia Canipe[2], James Caplinger[2], Francis Caputo[2], Larkin Carey[8], Stefano Carniani[19], Maria Carrasquilla[8], Margaret Carruthers[2], Michael Case[2], Don Chance[2], George Chapman[2], Stéphane Charlot[20], Brian Charlow[2], Pierre Chayer[2], Bin Chen[2], Brian Cherinka[2], Sarah Chichester[2], Zack Chilton[2], Taylor Chonis[8], Charles Clark[1], Kerry Clark[2], Dan Coe[2], Benee Coleman[2], Brian Comber[1], Tom Comeau[2], Dennis Connolly[1], Rachel Cooper[2], James Cooper[1], Eric Coppock[8], Matteo Correnti[2], Christophe Cossou[21], Alain Coulais[14], Laura Coyle[8], Misty Cracraft[2], Mirko Curti[22], Steven Cuturic[9], Katherine Davis[2], Michael Davis[1], Bruce Dean[1], Amy DeLisa[1], Wim deMeester[11], Nadia Dencheva[2], Nadezhda Dencheva[2], Joseph DePasquale[2], Jeremy Deschenes[2], Örs Hunor Detre[16], Rosa Diaz[2], Dan Dicken[5], Audrey DiFelice[2], Matthew Dillman[2], William Dixon[2], Jesse Doggett[2], Tom Donaldson[2], Rob Douglas[2], Kimberly DuPrie[2], Jean Dupuis[23], John Durning[1], Nilufar Easmin[2], Weston Eck[2], Chinwe Edeani[2], Eiichi Egami[6], Ralf Ehrenwinkler[10], Jonathan Eisenhamer[2], Michael Eisenhower[24], Michelle Elie[2], James Elliott[2], Kyle Elliott[2], Tracy Ellis[2], Michael Engesser[2], Nestor Espinoza[2], Odessa Etienne[2], Mireya Etxaluze[25], Patrick Falini[2], Matthew Feeney[2], Malcolm Ferry[26], Joseph Filippazzo[2], Brian Fincham[2], Mees Fix[2], Nicolas Flagey[2], Michael Florian[6], Jim Flynn[13], Erin Fontanella[2], Terrance Ford[1], Peter Forshay[2], Ori Fox[2], David Franz[1], Henry Fu[13], Alexander Fullerton[2], Sergey Galkin[2], Anthony Galyer[1], Macarena Garcia Marin[4], Lisa Gardner[2], Jonathan Gardner[1], Dennis Garland[2], Danny Gasman[11], Andras Gaspar[6], Daniel Gaudreau[23], Peter Gauthier[2], Vincent Geers[5], Paul Geithner[1], Mario Gennaro[2], Giovanna Giardino[27], Julien Girard[2], Mark Giuliano[2], Kirk Glassmire[2], Adrian Glauser[28], Stuart Glazer[1], John Godfrey[2], David Golimowski[2], David Gollnitz[2], Fan Gong[9], Shireen Gonzaga[2], Michael Gordon[8], Karl Gordon[2], Paul Goudfrooij[2], Thomas Greene[29], Matthew Greenhouse[1], Stefano Grimaldi[8], Andrew Groebner[2], Timothy Grundy[25], Pierre Guillard[20], Irvin Gutman[2], Kong Q. Ha[1], Peter Haderlein[17], Andria Hagedorn[13], Kevin Hainline[6], Craig Haley[9], Maryam Hami[2], Forrest Hamilton[2], Heidi Hammel[30], Carl Hansen[2], Tom Harkins[13], Michael Harr[2], Quyen Hart[2], Jessica Hart[2], George Hartig[2], Ryan Hashimoto[13], Sujee Haskins[1], William Hathaway[2], Keith Havey[1], Brian Hayden[2], Karen Hecht[2], Chris Heller-Boyer[2], Alaina Henry[2], Karl Hermann[10], Scarlin Hernandez[2], Brigette Hesman[2], Brian Hicks[8], Bryan Hilbert[2], Dean Hines[2], Melissa Hoffman[2], Sherie Holfeltz[2], Bryan J. Holler[2], Jennifer Hoppa[2], Kyle Hott[13], Joseph Howard[1], David Hunter[2], Alexander Hunter[2], Brendan Hurst[2], Bernd Husemann[16], Leah Hustak[2], Luminita Ilinca Ignat[23], Sandra Irish[1], Wallace Jackson[13], Amir Jahromi[1], Peter Jakobsen[31], LeAndrea James[2], Bryan James[1], William Januszewski[2], Ann Jenkins[2], Hussein Jirdeh[2], Phillip Johnson[2], Timothy Johnson[2], Olivia Jones[5], Danny Jones[2], Ron Jones[1], Vicki Jones[2], Ian Jordan[2], Margaret Jordan[2], Sarah Jurczyk[8], Alden Jurling[1], Catherine Kaleida[2], Phillip Kalmanson[2], Jens Kammerer[2], Huijo Kang[2], Shaw-Hong Kao[2], Diane Karakla[2], Patrick Kavanagh[32], Doug Kelly[6], Sarah Kendrew[4], Herbert Kennedy[2], Deborah Kenny[2], Ritva Keski-kuha[1], Charles Keyes[2], Richard Kidwell[2], Wayne Kinzel[2], Jeff Kirk[1], Mark Kirkpatrick[13], Danielle Kirshenblat[2], Pamela Klaassen[5], Bryan Knapp[2], J. Scott Knight[8], Perry Knollenberg[13], Robert Koehler[2], Anton Koekemoer[2], Aiden Kovacs[2], Trey Kulp[2], Nimisha Kumari[33], Mark Kyprianou[2], Stephanie La Massa[2], Aurora Labador[2], Alvaro Labiano Ortega[34], Pierre-Olivier Lagage[21], Charles-Phillipe Lajoie[2], Matthew Lallo[2], May Lam[2], Tracy Lamb[2], Scott Lambros[1], Richard Lampenfield[2], James Langston[2], Kirsten Larson[33], David Law[2], Jon Lawrence[1], David Lee[5], Jarron Leisenring[6], Kelly Lepo[2], Michael Leveille[2], Nancy Levenson[2], Marie Levine[17], Zena Levy[2], Hannah Lewis[2], Dan Lewis[26], Mattia Libralato[33], Paul Lightsey[8], Miranda Link[2], Lily Liu[2], Amy Lo[13], Alexandra Lockwood[2], Ryan Logue[2], Douglas Long[2], Chris Long[2], Charles Loomis[2], Marcos Lopez-Caniego[35], Jose Lorenzo Alvarez[4], Jennifer Love-Pruitt[13], Adrian Lucy[2], Nora Luetzgendorf[4], Peiman Maghami[1], Roberto Maiolino[22], Melissa Major[2], Sunita Malla[2], Eliot Malumuth[1], Elena Manjavacas[33], Crystal Mannfolk[2], Amanda Marrione[2], Anthony Marston[4], André Martel[2], Marc Maschmann[10], Gregory Masci[2], Michaela Masciarelli[8], Michael Maszkiewicz[23], John Mather[1], Kenny McKenzie[1], Brian McLean[2], Matthew McMaster[2], Katie Melbourne[8], Marcio Meléndez[2], Michael Menzel[1], Kaiya Merz[2], Michele Meyett[2], Luis Meza[13], Cherie Miskey[1], Karl Misselt[6], Christopher

Moller[1], Jane Morrison[6], Ernie Morse[2], Harvey Moseley[36], Gary Mosier[1], Matt Mountain[30], Julio Mueckay[8], Michael Mueller[37], Susan Mullally[2], Jess Murphy[8], Katherine Murray[2], Claire Murray[2], James Muzerolle[2], Matthew Mycroft[17], Richard Myers[13], Kaila Myrick[2], Shashvat Nanavati[13], Elizabeth Nance[2], Omnarayani Nayak[2], Bret Naylor[17], Edmund Nelan[2], Bryony Nickson[2], Alethea Nielson[1], Maria Nieto-Santisteban[2], Nikolay Nikolov[2], Alberto Noriega-Crespo[2], Brian O'Shaughnessy[2], Brian O'Sullivan[4], William Ochs[1], Patrick Ogle[2], Brenda Oleszczuk[2], Joseph Olmsted[2], Shannon Osborne[2], Richard Ottens[1], Beverly Owens[2], Camilla Pacifici[2], Alyssa Pagan[2], James Page[2], Keith Parrish[1], Polychronis Patapis[28], Tyler Pauly[2], Cheryl Pavlovsky[2], Andrew Pedder[2], Matthew Peek[2], Maria Pena-Guerrero[2], Konstantin Pennanen[17], Yesenia Perez[2], Michele Perna[12], Beth Perriello[2], Kevin Phillips[1], Martin Pietraszkiewicz[13], Jean-Paul Pinaud[13], Norbert Pirzkal[33], Joseph Pitman[38], Aidan Piwowar[9], Vera Platais[2], Danielle Player[2], Rachel Plesha[2], Joe Pollizi[2], Ethan Polster[2], Klaus Pontoppidan[2], Blair Porterfield[2], Charles Proffitt[2], Laurent Pueyo[2], Christine Pulliam[2], Brian Quirt[2], Irma Quispe Neira[2], Rafael Ramos Alarcon[2], Leah Ramsay[2], Greg Rapp[8], Robert Rapp[1], Bernard Rauscher[1], Swara Ravindranath[2], Timothy Rawle[4], Michael Regan[2], Timothy A. Reichard[1], Carl Reis[39], Michael E. Ressler[17], Armin Rest[2], Paul Reynolds[13], Timothy Rhue[2], Karen Richon[1], Emily Rickman[4], Michael Ridgaway[2], Christine Ritchie[2], Hans-Walter Rix[16], Massimo Robberto[2], Orion Robinson[2], Michael Robinson[2], Gregory Robinson[40], Frank Rock[2], David Rodriguez[2], Bruno Rodriguez Del Pino[41], Thomas Roellig[29], Scott Rohrbach[1], Anthony Roman[2], Fred Romelfanger[2], Perry Rose[2], Anthony Roteliuk[13], Marc Roth[13], Braden Rothwell[2], Neil Rowlands[9], Arpita Roy[2], Pierre Royer[11], Patricia Royle[2], Chunlei Rui[13], Peter Rumler[4], Joel Runnels[8], Melissa Russ[2], Zafar Rustamkulov[42], Grant Ryden[13], Holly Ryer[2], Modhumita Sabata[2], Derek Sabatke[8], Elena Sabbi[2], Bridget Samuelson[13], Bradley Sappington[2], B. Sargent[2,42], Arne Sauer[10], Silvia Scheithauer[16], Everett Schlawin[6], Joseph Schlitz[2], Tyler Schmitz[2], Analyn Schneider[17], Jürgen Schreiber[16], Vonessa Schulze[2], Ryan Schwab[2], John Scott[2], Kenneth Sembach[2], Bryan Shaughnessy[25], Richard Shaw[2], Nanci Shawger[13], Christopher Shay[2], Evan Sheehan[1], Sharon Shen[2], Allan Sherman[1], Bernard Shiao[2], Hsin-Yi Shih[2], Irene Shivaei[6], Matthew Sienkiewicz[2], David Sing[42], Marco Sirianni[4], Anand Sivaramakrishnan[2], Joy Skipper[2], Gregory Sloan[2], Christine Slocum[2], Steven Slowinski[2], Erin Smith[1], Eric Smith[40], Denise Smith[2], Corbett Smith[1], Gregory Snyder[2], Warren Soh[9], Tony Sohn[2], Christian Soto[2], Richard Spencer[2], Scott Stallcup[2], John Stansberry[2], Elysia Starr[13], Carl Starr[1], Alphonso Stewart[1], Massimo Stiavelli[2], Amber Straughn[1], David Strickland[2], Jeff Stys[2], Francis Summers[2], Fengwu Sun[6], Ben Sunnquist[2], Daryl Swade[2], Michael Swam[2], Robert Swaters[2], Robby Swoish[13], Jo Taylor[2], Rolanda Taylor[2], Maurice Te Plate[4], Mason Tea[2], Kelly Teague[2], Randal Telfer[2], Tea Temim[43], Deepashri Thatte[2], Linda Thompson[2], Christopher Thompson[2], Shaun Thomson[1], Tuomo Tikkanen[44], William Tippet[2], Connor Todd[2], Sharon Toolan[2], Hien Tran[2], Edwin Trejo[2], Justin Truong[2], Chris Tsukamoto[13], Samuel Tustain[25], Harrison Tyra[2], Leonardo Ubeda[2], Kelli Underwood[2], Michael Uzzo[2], Julie Van Campen[1], Thomas Vandal[3], Bart Vandenbussche[11], Begoña Vila[1], Kevin Volk[2], Glenn Wahlgren[2], Mark Waldman[1], Chanda Walker[8], Michel Wander[23], Christine Warfield[2], Gerald Warner[9], Matthew Wasiak[1], Mitchell Watkins[2], Mark Weilert[17], Nick Weiser[8], Ben Weiss[13], Sarah Weissman[2], Alan Welty[2], Garret West[8], Lauren Wheate[1], Elizabeth Wheatley[2], Thomas Wheeler[2], Rick White[2], Kevin Whiteaker[8], Paul Whitehouse[1], Jennifer Whiteleather[2], William Whitman[2], Christina Williams[6], Christopher Willmer[6], Scott Willoughby[13], Andrew Wilson[9], Gregory Wirth[8], Emily Wislowski[2], Erin Wolf[8], David Wolfe[2], Schuyler Wolff[6], Bill Workman[2], Ray Wright[8], Rai Wu[2], Carl Wu[1], Kristen Wymer[2], Kayla Yates[2], Jared Yates[9], Christopher Yeager[2], Ethan Yerger[2], Jinmi Yoon[2], Alice Young[4], Susan Yu[2], Dean Zak[2], Peter Zeidler[33], Julia Zhou[9], Thomas Zielinski[1], Cristian Zincke[1], Stephanie Zonak[2]

1: NASA's Goddard Space Flight Center. 2: Space Telescope Science Institute. 3: Université de Montréal. 4: European Space Agency. 5: UK Astronomy Technology Centre. 6: University of Arizona. 7: National Research Council Canada (Herzberg). 8: Ball Aerospace. 9: Honeywell International. 10: Airbus Defence and Space GmbH. 11: Katholieke Universiteit Leuven. 12: INTA/CSIC. 13: Northrop Grumman Space Systems. 14: Observatoire de Paris. 15: Niels Bohr Institute. 16: Max-Planck-Institut für Astronomie. 17: Jet Propulsion Laboratory. 18: University of Oxford. 19: Scuola Normale Superiore di Pisa. 20: Institut d'Astrophysique de Paris. 21: Commissariat à l'énergie atomique et aux énergies alternatives. 22: University of Cambridge. 23: Canadian Space Agency. 24: Center for Astrophysics | Harvard & Smithsonian. 25: Rutherford Appleton Laboratory. 26: Lockheed Martin Advanced Technology Center. 27: ATG Europe for the European Space Agency. 28: Eidgenössische Technische Hochschule. 29: NASA's Ames Research Center. 30: Association of Universities for Research in Astronomy. 31: University of Copenhagen. 32: Dublin Institute for Advance Studies. 33: AURA for the European Space Agency. 34: Telespacio for the European Space Agency. 35: Aurora Technology for the European Space Agency. 36: Quantum Circuits. 37: University of Groningen. 38: Heliospace. 39: NASA's Johnson Space Center. 40: National Aeronautics and Space Administration. 41: Centro de Astrobiología- Instituto Nacional de Técnica Aeroespacial. 42: John Hopkins University. 43: Princeton University. 44: University of Leicester.

Contents

1.0 Introduction and Executive Summary

This document characterizes the actual science performance of JWST, as known on 12 July 2022.

During the six-month commissioning period of JWST, the mission team worked with dedication and focus to prepare the observatory for science operations. A key part of commissioning activities was characterizing the on-orbit performance of the observatory. This document summarizes those results, drawn from many activities and analyses over the past six months.

The design and architecture of JWST, and pre-launch predicted performance, are described elsewhere. This document summarizes what was actually delivered, and how the actual performance differs from pre-launch expectations. We summarize in turn the performance of the spacecraft, telescope, science instruments, and ground system. Further details will appear in a planned series of papers in a PASP special issue on JWST.

The key outcome of six months of commissioning is this: JWST is fully capable of achieving the discoveries for which it was built. JWST was envisioned "to enable fundamental breakthroughs in our understanding of the formation and evolution of galaxies, stars, and planetary systems" (Gardner et al. 2006) — we now know with certainty that it will. The telescope and instrument suite have demonstrated the sensitivity, stability, image quality, and spectral range that are necessary to transform our understanding of the cosmos through observations spanning from near-earth asteroids to the most distant galaxies.

Moreover, almost across the board, the science performance of JWST is better than expected. The optics are better aligned, the point spread function is sharper with higher encircled energy, and the optical performance is more time-stable than requirements. The fine guidance system points the observatory several times more accurately and precisely than required. The mirrors are cleaner than requirements, which translates into lower-than-expected levels of near-infrared stray light, meaning that the <5 μm sky background will be darker for JWST than expected. The science instruments have generally higher total system throughput than pre-launch expectations. Detector noise properties are similar to ground tests, albeit with higher rates of cosmic rays, as expected in deep space. Collectively, these factors translate into substantially better sensitivity for most instrument modes than was assumed in the exposure time calculator for Cycle 1 observation planning, in many cases by tens of percent. **In most cases, JWST will go deeper faster than expected.** In addition, JWST has enough propellant onboard to last at least 20 years.

Commissioning proved the observatory's capabilities through approximately 2300 visits of commissioning observations, which exercised the same science instrument modes that will be used in normal science operations. All four science instruments have demonstrated the ability to precisely capture spectra of transiting exoplanets with initial precision better than 100 ppm per measurement point, with limiting performance expected to be well below that level[1]. JWST has tracked solar system objects at speeds up to 67 milliarcseconds/second, more than twice as fast as the requirement. JWST has detected faint galaxies with fluxes of several nano-Jansky, and observed targets as bright as Jupiter. JWST has obtained infrared spectra of hundreds of stars simultaneously in a dense starfield toward the Galactic center, as well as integral field spectroscopy of planetary nebulae and a Seyfert nucleus at unprecedented sensitivity. Data from these and all other commissioning activities will be available to the scientific

[1]That time series precision of < 100 ppm is measured at spectral resolutions of R=100 at wavelengths below 5 μm and R=50 at longer wavelengths, with minimal detrending.

community via the MAST archive starting July 14.

JWST has 17 science instrument modes. As each mode finished its commissioning activities, it was reviewed against mode-specific readiness criteria for science instrument performance. **As of 2022 July 10, all JWST observing modes have been reviewed and confirmed to be ready for science use.** The performance of each science mode is described below. In most cases, the modes surpass performance requirements.

An initial set of updates to the JDox documentation system have been published simultaneously with this document; for many topics discussed below, JDox has more detailed information. Continued analyses as well as Cycle 1 calibrations will further improve the characterization of the science instruments. Updated knowledge will be reflected in updates to data pipeline reference files and algorithms, as well as thorough revisions to the JDox documentation and updates to the JWST proposal tools that will be timed to support the Cycle 2 Call for Proposals[2]. A series of papers describing on-orbit performance is planned, as noted above. For now, this document summarizes our best understanding of the science performance that has been achieved.

The authors acknowledge the tremendous amount of work by the entire international mission team to bring JWST through commissioning into science operations. The scientific performance of JWST is the result of efforts spanning decades by thousands of individuals from multiple institutions.

2.0 Spacecraft

2.1 Orbit

The Ariane 5 rocket that launched JWST on 2021 Dec 25 UT injected it into an orbit that was well within specification, with a semi-major axis approximately 0.5 sigma larger than nominal. This very slightly "hot" injection state had a semi-major axis of 542120.1 km versus the nominal of 536533.8 km, and a delta-v at launch vehicle separation within 3 m/s of the target velocity of 10,089 m/s. This accurate launch, in combination with three on-time, nominal mid-course corrections, minimized propellant consumption and delivered JWST to a nominal orbit around the second Earth-Sun Lagrange point (L2). This orbit fully complies with all geometry requirements, and supports communications with the Science & Operations Center using the Deep Space Network.

Orbit around L2 is maintained through regular station-keeping burns, which are scheduled every three weeks. As of July 12, 2022, there have been four station-keeping burns, with typical durations of tens of seconds. During commissioning, three station-keeping burns were skipped because the computed correction was negligibly small.

2.2 Predicted lifetime of consumables

There are no consumable cryogens onboard JWST; the telescope and the science instruments are passively cooled by the sunshield and radiators, and MIRI's active cryocooler recycles its helium. The only onboard consumables are propellant: fuel and oxidizer. Before launch, JWST was required to carry propellant for at least 10.5 years of mission lifetime. Now that JWST is in orbit around L2, it is clear that the remaining propellant will last for more than 20 years of mission lifetime. This fortunate surfeit has multiple causes: an accurate launch; launch on a day that required relatively less energy to get to L2 than most other possible launch dates; three timely and accurate mid-course corrections that sent JWST to L2 with the

[2] The Cycle 2 Call for Proposals is planned to be released in Nov. 2022, with proposals expected to be due in Jan. 2023.

minimum possible propellant usage; and finally, careful stewardship of mass margins by the engineering team over the years, such that the remaining mass margin was used to add more propellant than required, until the tanks were full.

For the remainder of the mission, propellant will be used for two purposes: stationkeeping burns (using fuel and oxidizer) to maintain the orbit around L2, and momentum dumps (using only fuel) to remove momentum from the reaction wheels. Momentum accumulates as solar photons hit the sunshield and impart a net torque, which the reaction wheels resist by spinning up. The actual rate at which the observatory builds up momentum is within specifications and is well below worst-case allocations, which further contributes to propellant lifetime. While the detailed propellant usage depends on orientation, which is set by the observing schedule, the big picture is that JWST has sufficient propellant onboard to support science operations for more than 20 years.

2.3 Projected observatory lifetime

At this point, it is not clear what will determine the duration of JWST's mission. The mirrors and sunshield are expected to slowly degrade from micrometeoroid impacts; the detectors are expected to experience cumulative slow damage from charged particles; the sunshield and multilayer insulation will degrade from space weathering; the spacecraft was designed for a five year mission (as is standard for NASA science missions); and the science instruments include many moving parts at cryogenic temperatures. These sources of degradation were all taken into account in the design of JWST, with performance margins set so that JWST will still perform after many years of operation. At present, the largest source of uncertainty is long term effects of micrometeoroid impacts that slowly degrade the primary mirror. As discussed in Section 4.6, the single micrometeorite impact that occurred between 22—24 May 2022 UT exceeded prelaunch expectations of damage for a single micrometeoroid[3], triggering further investigation and modeling by the JWST Project. The Project is actively working this issue to ensure a long, productive science mission with JWST.

2.4 Slew speed and settle times

The slew speed and settle time are important drivers for efficient operations as the observatory changes pointing to look at different targets on sky and carry out orbital stationkeeping and momentum unloading maneuvers. Slews use all six reaction wheels on the spacecraft to repoint the observatory, although it is possible to control with five reaction wheels. The control system was designed to slew 90 degrees in less than 60 minutes, which has been demonstrated during commissioning.

Achieved slew speeds and durations to repoint to new targets at the start of each visit are broadly consistent with pre-flight expectations, such as the timing model encoded in APT, plus typically 2 minutes duration for control overheads and settling.

At the end of a slew, pointing transients are observed while the observatory settles. The pointing settles in ~30 s with damping from isolators between the telescope and spacecraft bus. Re-pointing maneuvers can generate fuel slosh, which is at ~0.045 Hz and not compensated by the fine guidance control system. The slew rate profile has been tuned to reduce the excitation of the fuel slosh mode. Measurements of line-of-sight pointing performance (section 3.3 below) confirm that the resulting effect of fuel slosh on

[3] Pre-launch projections, informed by micrometeoroid population models and experimental studies and numerical simulations of impacts to beryllium mirrors, predicted that on average each segment would receive a cumulative total of 16 nm added WFE over six years. The May impact resulted in one segment receiving more than 10 times that average in a single event.

pointing is < 0.5 milliarcseconds.

After slewing to a new target, the pointing stabilizes quickly in less time than it takes the FGS guide star acquisition process to complete. This was not initially the case; in the first months of commissioning, long slew settling times and high image motion impacted many observations, and required efforts to investigate, diagnose, and mitigate. Adjustments to Attitude Control System parameters and several software patches dramatically improved slew settling performance and resolved this issue. Users examining very early commissioning data (prior to mid-April 2022), particularly images taken in coarse point mode without fine guiding, should be aware of this caveat.

2.5 Thermal

The cooldown of the telescope and science instruments was nominal and closely matched predictions. As predicted, the primary mirror segments have cooled to temperatures of 35—55 K, with the hotter segments those closest to the sunshield. The secondary mirror has cooled to 29.3 K, the near-IR instruments to 35—39 K, and MIRI to 6.4 K. The MIRI cooler achieves this temperature at nominal, pre-flight predicted performance levels and has no perceptible effect on pointing stability (e.g., jitter) or on the performance of the other instruments. Since cooling to operational temperatures two months ago, these temperatures have remained extremely stable with time. For the telescope mirrors and structures, the stability is within the 40 mK noise of the temperature sensors on those components. The science instrument temperatures vary based on their activity, but they are also within the 10 mK noise for the instrument sensors. Any resulting temperature change impact can only be identified optically (see Section 4.5). No long term temperature drift has been detected during the two months since achieving final cooldown conditions. Temperatures of detector focal plane arrays are actively stabilized to a precision of a few mK.

The observatory was designed to minimize ice deposition on the optical surfaces. Sensitive components of the science instruments and the telescope's fine steering mirror were heated through the cooldown to prevent ice accumulation. Throughput measurements detect no spectral signatures of ice, which constrains any ice deposition that may have occurred to be far better (less ice) than the requirements.

Components within the spacecraft bus (computer, communications, cryocooler compressors & electronics, attitude control & propulsion systems, etc.) are comfortably within required operating temperature ranges regardless of pointing direction or telescope activities. Instrument electronics housed on the cold side of the Observatory are also within required operating range and are under tight temperature control to minimize any temperature-induced distortions (see Section 4.5.3). All heaters on the observatory are functional on prime circuits and demonstrating expected margins.

2.6 Sunshield performance

The shape of the deployed sunshield affects the temperature and thermal stability of JWST, the amount of scattered light from the Earth, Moon, and stars, and the background levels at the longer wavelengths. Telemetry (microswitch, motor, thermal, power, and inertial reference unit) indicated a successful deployment ending with a nominal deployed shape. There are no subsequent indications of any issue with the deployed shape, from the many thermal sensors onboard or from the background levels seen in the science instruments.

The shape of the deployed sunshield affects how quickly the observatory builds up angular momentum from solar photons, which is then stored in the reaction wheels and must be dumped periodically using thrusters. The sunshield geometry was designed to minimize momentum accumulation. The measured

torque table on-orbit is consistent with the pre-launch model within the allocated uncertainties. As noted above, this implies a lower rate of fuel use for momentum management.

2.7 Other spacecraft performance

After optimization of the solar array regulator settings, JWST is now generating 1.5 kW to match the power load, with a capability of > 2 kW — as such, the power margins are comfortable. JWST is projected to have a tight (11%) margin on data downlink during Cycle 1. The project is working closely with DSN to resolve all issues and ensure DSN can adequately support all Cycle 1 science and beyond. The JWST spacecraft has all the redundancy it had at launch. Of the 344 single point failures at launch, almost all of them related to deployments, only 49 remain; these are common to most science missions (for example, only one set of propellant tanks, only one high gain antenna). Fifteen of the remaining single point failure items are associated with the science instruments — any future failure with these items would degrade science performance but would not end the mission.

2.8 Fault management

JWST has a robust fault management system that makes use of its redundant components to ensure the observatory remains safe. With any new spacecraft/observatory, the first couple months after launch provide the operations team an opportunity to learn how the vehicle performs on-orbit and adjust the fault management and system parameters to fine tune the system behavior. JWST has experienced seven safe mode entries (six safe haven and one inertial point mode) since launch. The majority of these safe mode entries were a result of on-orbit learning of the nuances of the control system behavior and system level interactions. All of the safe mode entries' underlying causes are understood and several updates to the fault management and control system set items have been loaded to flight software to prevent the issues from recurring.

Likewise, flight software has placed individual instruments into safe modes on several occasions in responses to unexpected telemetry values or conflicting commands. In all cases the underlying issues were quickly understood, and appropriate steps were taken to bring the instrument back into operation and prevent recurrence of the fault. JWST's onboard event-driven operations system works as intended to allow the observatory to flexibly continue observations when an observation cannot execute due to an instrument fault or a guide star acquisition error; in such cases, JWST will automatically move on to the next observation in the onboard observation plan.

3.0 Pointing and guiding

Observatory attitude control and line-of-sight stabilization to achieve JWST's stringent requirements present a complex engineering challenge, involving a sophisticated interplay between hardware systems across the entire observatory and arguably the most complex set of flight software components. Line-of-sight pointing control with JWST requires the interconnected operation of star trackers, inertial reference units (gyroscopes), fine sun sensors, reaction wheels, the telescope's fine steering mirror, the fine guidance sensor, various target acquisition modes in science instruments, flight software in both the spacecraft and science instrument computers, and ground software systems for guide star selection and observation planning, as well as the structural dynamics of the deployed observatory.

It is inherently not possible to test those systems together in an end-to-end fashion on the ground. As such, on-orbit performance offers the first chance to characterize the system as a whole. As

commissioning concludes, the pointing performance of the observatory meets or exceeds expectations.

3.1 Pointing accuracy after guide star acquisition

Absolute pointing accuracy after guide star acquisition is excellent. Observed pointing offsets are generally below 0.19" (1-sigma, radial). When systematic offsets are removed by improved astrometric calibration between the Guiders and the other SIs, the residual scatter around the desired target position is generally below 0.10" (1-sigma, radial) , better than the prelaunch predicted value of 0.14", which is in turn significantly better than the required value of 1.0". Updates for such systematic offsets are in progress. This confirms expectations that many IFU spectroscopy observations will be able to omit target acquisition and rely solely on guide star acquisition to achieve the necessary science pointing. The excellent pointing performance can be credited to JWST's own systems, as well as the high accuracy and precision of the guide star catalog enabled by the Gaia mission.

Early in commissioning, some observations had significantly larger pointing offsets, of order ~1.5 arcsec, due to catalog cross-matching issues that occurred when data from Gaia and other catalogs such as 2MASS were combined to produce the current JWST guide star catalog. Updated guidelines for selecting guide/reference stars was implemented 5 May, and non-stars were disallowed as reference objects 24 June; both greatly reduced mis-identification. A future version of the catalog (late July) is expected to provide further improvements.

Pointing repeatability is likewise excellent: independent separate observations returning to the same target and at the same position angle generally result in identical target pointings on a detector to within < 0.1".

3.2 Pointing accuracy after target acquisition

For observing scenarios requiring better final pointing accuracy than provided by the guide star catalog alone, the instruments offer onboard Target Acquisition procedures to place targets where desired within an SI field, e.g. centered on a coronagraphic spot or null, or in a repeatable position for NIRISS Aperture Masking Interferometry or Single Object Slitless Spectroscopy. There are several distinct versions of target acquisition for the various instrument modes. These onboard processes have been confirmed to meet their requirements, typically yielding target positions within a few mas rms per axis in the near-IR instruments, and slightly larger in MIRI with its broader longer-wavelength PSFs. NIRCam coronagraphy, the final mode to have its Target Acquisition process evaluated, currently experiences larger offsets, which will be alleviated by future calibrations – even so, the Small Grid Dithers recommended for that mode cover the range of uncertainty and yield excellent coronagraphic contrast.

The algorithm for NIRSpec Multi-Object Spectroscopy is the most complex, because it derives a roll correction for the observatory position angle as well as the usual X,Y positional offsets. That procedure requires great care in implementation, and was the most challenging type of target acquisition to get working during commissioning, but with the requisite attention to the accuracy of the input reference data, that algorithm also meets its requirements.

3.3 Guiding precision and line of sight pointing stability

The pointing stability of the line of sight under fine guidance control is superb, several times better than requirements. The FGS sensing precision, parameterized as the Noise Equivalent Angle (NEA, an equivalent jitter angle calculated based on centroid precision and SNR) is usually ~ 1 mas (1 sigma per axis), as compared to the requirement of 4 mas; the NEA is usually symmetric in x and y.

The achieved line-of-sight jitter as seen in the science instruments is similarly good, even when measured at higher frequency than the 15.6-Hz cadence of the FGS measurements used in calculating the Guider NEA. Jitter measured via high-frequency sampling (every 2.2 milliseconds) using a small NIRCam subarray has also been ~1 mas (1 sigma per axis). For long observations, drift in observatory roll could generate systematic motion of sources in an SI field, as the FGS can not sense or correct roll with the single guide star used in the Fine Guide control loop. However, measurements during a commissioning thermal characterization test indicated that the roll drifts are extremely small, far below requirements, even after a worst-case hot-to-cold slew, and contribute negligibly to the total pointing error. In comparison, pre-flight predictions for pointing stability were in the range 6–7 mas (1 sigma per axis).

The FGS guide star magnitude scale matches the 2MASS J-band, Vega scale, with guide star brightnesses of $12.5 < J < 18$ allowed for fixed targets. Dimmer stars will typically have a larger NEA, due to the lower signal to noise per time step, but with NEA that is still well within the requirement. The guide star selection system preferentially selects the brightest available guide star for a given pointing. In practice the achieved NEA can vary by ~0.3 mas between dithers on the same source. For moving targets, the guide star faint limits are somewhat reduced to 16.5 in Guider 1 and 17.0 in Guider 2. Guiding performance can vary under some circumstances. Reasons that can cause a brighter star to appear to register lower counts than expected (and give an increased NEA) include: unflagged bad pixels in the guider box, (flagged) bad pixels exactly coincident with the guider star's position, guiding on an extended galaxy instead of a star, quantum efficiency variations due to cross hatching on the detector surface, or a guidestar falling at the edge of the centroiding box. Work is in progress to reduce these variations. In most cases, observers should expect excellent stability in their observations.

Very precise flight jitter measurements have yielded detailed insights into observatory dynamics, and confirmed many aspects of preflight integrated modeling. These data show that neither the spacecraft's reaction wheels nor the MIRI cryocooler produce measurable contributions to the line-of-sight jitter. Instead there are two signatures, detectable but at low level, that come from a 0.3 Hz oscillation mode of a vibration damper between the telescope and spacecraft bus, and a ~0.045 Hz oscillation understood to be due to fuel slosh, both consistent with models. The amplitudes of these modes range up to ~0.3 mas each, with variation over time that does not appear correlated with pointing history such as slew distances.

Momentum/reaction wheel operations or unplanned High Gain Antenna motion may occasionally disturb observatory dynamics and degrade pointing stability; these are generally short-lived and fine guiding is expected to be maintained. High Gain Antenna moves are not planned during any science observations except for long duration time series observations.

3.4 Precision of dithering

JWST has three methods of performing a small repointing, commonly called a dither. Dithers less than 60 mas are executed with the fine steering mirror (FSM) while maintaining closed loop on the guide star. Dithers between 60 mas and 25 arcsec are executed by dropping closed-loop guiding, slewing, and re-entering guiding at the track mode stage. Dithers larger than 25 arcsec are executed by dropping closed-loop guiding, slewing, and re-entering guiding at the guide star acquisition stage.

All three methods of dithers result in an offset precision as measured by the Guider of 1–2 mas. On the sky, the accuracy of the dithers is typically 2–4 mas rms per axis, due to residuals in the Guider's astrometric calibration or small systematic offsets in the Guider's calculated 3x3-pixel centroids. As reported by the observing SI, offsets for large dithers may differ by another few mas, due to residuals in the astrometric calibration of the SI. As SI astrometric calibrations continue to improve, these residuals

may decrease.

3.5 Performance for tracking moving targets

JWST has a Level 1 requirement to track objects within the solar system at speeds up to 30 milliarcseconds per second (mas/s). In commissioning, tracking was tested at rates from 5 mas/s to >67 mas/s. These tests verified tracking and science instrument performance for moving targets, including dithering and mosaicking.

All tests of moving targets during commissioning were successful. Centroids showed sub-pixel scatter in all instruments. No test showed elongation of moving targets, as would be expected in the case of poor tracking. RMS jitter in the guider was typically <2 mas (1-sigma, radial), comparable to that seen for fixed targets. Image quality as determined by FWHM measurements of point spread functions was also comparable to that of fixed targets. Table 1 summarizes the moving targets observations during commissioning.

Tracking at faster-than-spec rates of 30–67 mas/s showed accuracies similar to tracking of slower-moving targets; this potentially opens up science for near-Earth asteroids (NEAs), comets closer to perihelion, and interstellar objects. Tracking at these faster rates of motion is expected to be enabled in future observing cycles.

Moving target	Apparent Rate of Motion (mas/s)	Program ID	Instrument/Mode
Jupiter	3.3	1022	NIRCam Imaging, NIRISS Imaging, NIRSpec fixed slits and IFU, MIRI MRS and imaging
2516 Roman	4.7	1449	MIRI/Imaging
118 Peitho	4.9	1449	MIRI/ LRS and MRS
6481 Tenzing	5	1021	NIRCam/Imaging
1773 Rumpelstilz	6.6	1021	NIRISS/AMI
216 Kleopatra	11	1444	NIRSpec/ IFU and MOS longslit
2035 Stearns	24	1021	NIRCam/Imaging
4015 Wilson-Harrington	40	1021	NIRCam/Imaging
2004 JX20	67	1021	NIRCam/Imaging

Table 1: Moving targets tested during commissioning. *Targets are sorted by apparent rate of motion.*

Observing a bright planet and its satellites and rings was expected to be challenging, due to scattered light that may affect the science instrument employed, but also the fine guidance sensor must track guide stars

near the bright planet. Therefore, commissioning included tests of moving target tracking with NIRCam, where Jupiter was incrementally moved from the NIRCam field of view (FOV) to the FGS-2 FOV. See Figure 1. These observations verified the expectation that guide star acquisition works successfully as long as Jupiter is at least 140" away from the FGS, consistent with pre-flight modeling.

The other SIs were also tested for efficiency with nearby scattered light, also using the Jupiter system. Preliminary results have measured scattered light contamination on the detectors for all instruments when the planet was not in the primary FOV, which will need to be considered for planning nearby satellite observations.

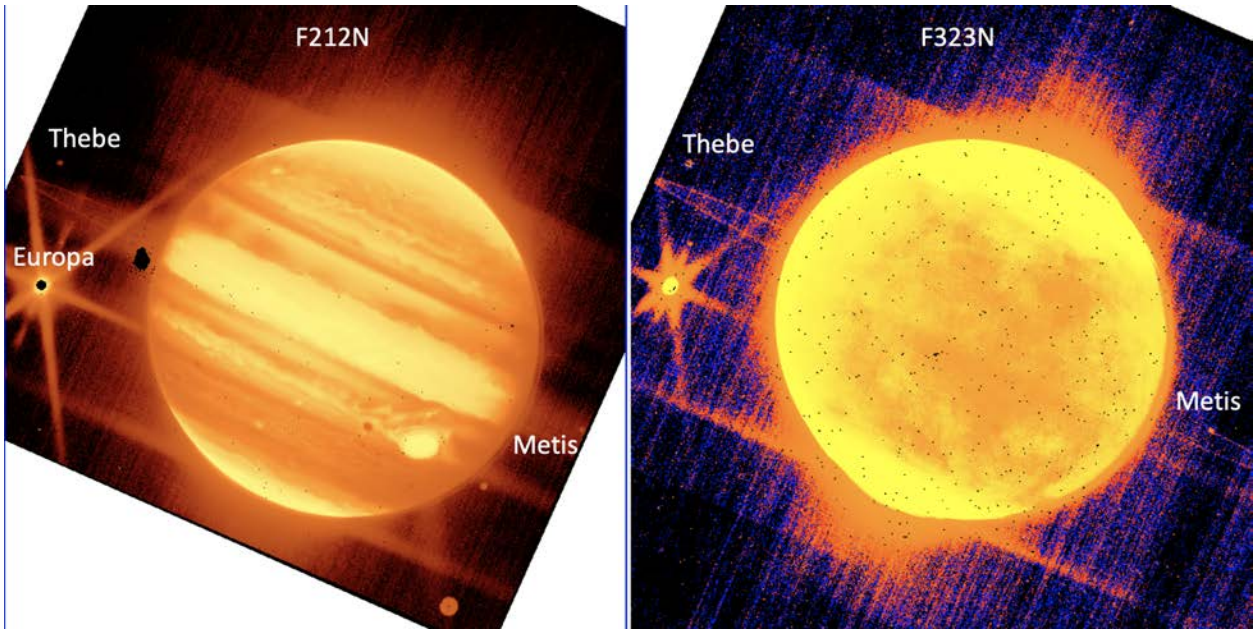

Figure 1: NIRCam narrow-band imaging of Jupiter, moons, and ring. *PID 1022 demonstrated that JWST can track moving targets even when there is scattered light from a bright Jovian planet. At left is a NIRCam short-wavelength image in filter F212N (2.12 μm); at right is a NIRCam long-wavelength image in filter F323N (3.23 μm). The exposure time was 75 s. The Jovian moons Europa, Thebe, and Metis are labeled. The shadow of Europa is also visible, just to the left of the Great Red Spot. The stretch is fairly harsh to bring out the faint moons as well as Jupiter's ring.*

3.6 Success rate for closed-loop guiding

The closed-loop fine guidance system is one of the most complex aspects of JWST operations, requiring close coordination between several subsystems and multiple control loops running in real time. Activating and tuning the fine guidance system was a significant focus during commissioning. The robustness of the system has steadily improved and continues to do so as reasons for failure are identified and mitigated.

As a snapshot of performance during the later period of commissioning, from 25 May through 16 June 2022, guiding worked successfully ~93% of the time: guiding was successful on the first try ~81% of the time, and 12% of the time succeeded on the second or third guide star candidate attempted. (Up to three guide star candidates can be tried in a visit.) In the same time period, guiding failed or skipped 7% of the

time.

Several reasons for guiding failure were identified, with steps taken to mitigate them:

- The "guidestar" is actually a galaxy, but was classified as a star in the guide star catalog. These are flagged in the guide star catalog once found.
- Attempts to guide on known galaxies frequently failed. Using a known galaxy as a reference source for ID was disallowed starting 24 June.
- Guide star coordinates, or occasionally brightnesses, in the catalog are incorrect. The catalog is corrected when such errors are found.
- The guide star catalog contained duplicate entries for some guide stars. This duplication was reduced greatly with new rules for selecting guide stars, implemented 5 May 2022. A new version of the guide star catalog expected in late July 2022 should largely eliminate this issue.
- The guide star may be placed on a bad pixel. Bad pixels are flagged once identified.
- The pointing may not have stabilized sufficiently at the start of the Guide Star ID process.

In Cycle 1, users should expect a closed-loop guiding success rate close to the 93% value that was achieved late in commissioning. That value is, largely by coincidence, very close to the success rate for Hubble guide star acquisitions in recent cycles. Efforts continue to optimize guiding success rates.

4.0 Optical performance

The image quality achieved by JWST exceeds performance requirements and expectations, having diffraction-limited image quality at wavelengths much lower than requirements, very good stability, and superb throughput. There is not one single factor to credit for the high performance; rather it is the accumulation of performance margins throughout the observatory, and the result of many careful and precise efforts throughout the design, assembly, and alignment of the telescope and instruments. JWST's requirement was to be diffraction-limited at λ=2 μm wavelength, defined as λ/14 or 150 nm wavefront error, with a Strehl ratio of 0.8. In fact, the observatory is correctable to ~80 nm wavefront error, which means it is diffraction-limited at 1.1 μm. Other documents will describe in more detail the telescope deployment and alignment processes as carried out in flight. Here we summarize the achieved optical performance, drawing on extensive telescope wavefront sensing and image characterizations throughout commissioning, including a dedicated thermal stability characterization exercise.

4.1 Wavefront error and angular resolution

The achieved telescope wavefront error (WFE), measured at the primary wavefront sensing field point in NIRCam module A, is generally in the range 60–80 nanometers rms; it varies on multiple timescales as described below[4]. That WFE contribution sums with field-dependence of the telescope WFE and instrument internal WFE to yield total observatory WFE values which are modestly higher: 75–130 nm depending on instrument, observing mode, and field position. See Table 2. Motions of mirror segments over time can lead occasionally to wavefront error levels higher than those values, which are corrected through the routine wavefront sensing and control process.

JWST has exquisite image quality across the entire telescope field of view and at all available wavelengths. Expressed relative to wavelength λ, JWST ranges from ~λ/10 for NIRCam F070W to better

[4] The best achieved telescope wavefronts at the completion of alignment were as low as 50 nm rms; the May 2022 micrometeoroid impact on segment C3 subsequently raised the high-order uncorrectable WFE term enough that the floor is now 59 nm rms.

than λ/100 for MIRI F1000W and longer. JWST aimed to achieve at λ=2 μm a Strehl ratio of 0.8 (corresponding to wavefront rms λ/14 or better), which is considered having diffraction-limited image quality for space-based telescopes. This is achieved with substantial margin, such that the NIRCam SW channel, with typical WFE ~ 80 nm, in fact achieves λ/14 at λ=1.1 μm.

That wavefront quality yields optical point spread functions (PSFs) with angular resolutions set by the diffraction limit (i.e. PSF full width at half maximum ~ λ/D) across the full range of available wavelengths. See Figure 2. In particular, even in its shortest filter F070W, the NIRCam SW channel achieves a Strehl ratio of ~0.6. Though ~40–50% of the light is in a diffuse speckle halo at that wavelength, the PSF prior to detector sampling still has a tight core with angular resolution ~ λ/D. (In that sense, JWST's PSF quality at 0.7 μm is similar to PSFs achieved at 2 μm by adaptive optics systems on 8–10 m ground-based telescopes in good conditions.) In practice, angular resolution at the shortest wavelengths (< 2 μm for NIRCam SW, < 4 μm for NIRCam LW or NIRISS) is limited more significantly by detector pixel Nyquist sampling than by optical performance; subpixel dithering and image reconstruction ("drizzling") will be required to make use of the full resolution at these wavelengths[5].

Wavefront sensing confirms the surface quality of the individual mirror segments in space matches closely the mirror surface maps measured during cryogenic testing on the ground. See Figure 3. In other words, after launch into space, and significant thermal contraction and deformation while cooling from room temperature to ~45 K, the achieved wavefronts on each segment were just as expected.

Instrument	Measured Observatory Static WFE [nm rms]
NIRCam, short-wavelength	61 ± 8 (module A), 69 ± 11 (module B)
NIRCam, long wavelength	134 ± 38 (module A) 134 ± 39 (module B)
NIRISS	68 ± 12
NIRSpec	110 ± 20
MIRI	99 ± 28
FGS	77 ± 15 (FGS1), 69 ± 8 (FGS2)

Table 2: Measured static wavefront errors after Multi-Instrument Alignment. *Quoted values are the average over multiple field points within each instrument, as measured from Multi-Instrument Multi Field sensing during commissioning in May 2022, and updated for the final focus adjustment at the end of that process. The plus and minus ranges reflect the measured variation in wavefront error at different field points within each instrument's field of view. These values represent just the static (non-time-varying) portion of the wavefronts, and include the sum of telescope and instrument WFE together. Additional time-dependent terms sum on top of these*

[5] For example, in NIRCam's shortest filter F070W, the optical PSF pre-sampling is roughly 28 milliarcsec ~ 0.9 NIRCam SW pixels, but after sampling onto the detector pixel scale of 32 milliarcsec, the apparent PSF resolution becomes 40 milliarcsec ~ 1.25 NIRCam SW pixels.

at any given time. Data from PID 1465.

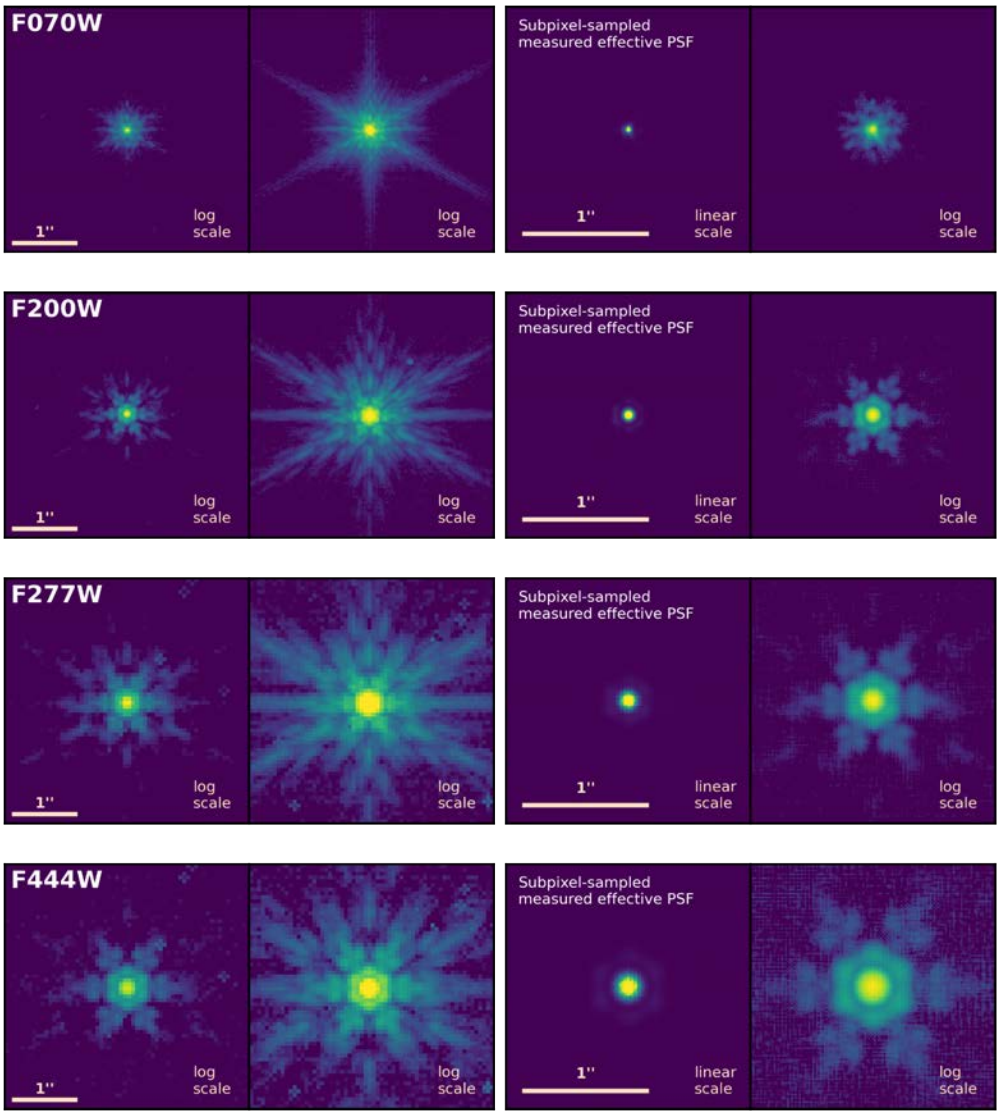

Figure 2: Measured Point Spread Functions spanning the full wavelength range of NIRCam. *The filters shown are the shortest and longest wide filters in each of the NIRCam SW and LW channels. The left two panels show individual PSFs (single exposure each), on two different logarithmic scales for higher dynamic range. The right two panels show 4x subsampled effective PSFs (ePSFs), generated following the method of Anderson & King (2000) using dithered PSF measurements of many stars; these are shown zoomed in by 2x compared to the left panels. The second column from right, shown on a linear scale, highlights the compact PSF core, while the log display in the other columns emphasizes the diffraction features from the primary mirror geometry. The PSF core is sharp even at the shortest wavelengths in F070W. Data from PIDs 1067 and 1072.*

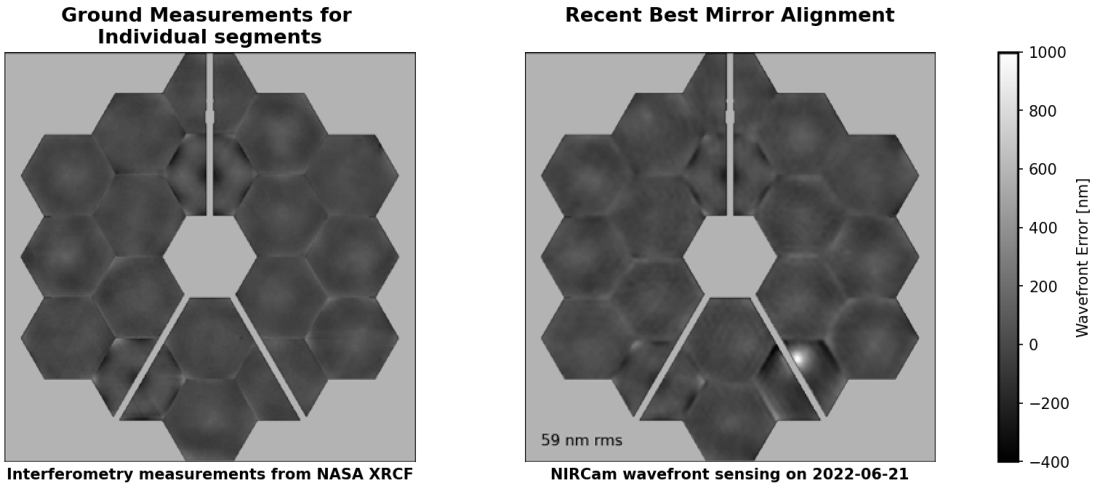

Figure 3: Wavefront Sensing Measurements showing the quality of achieved mirror alignment on orbit. *The telescope wavefront error achieved in flight, shown in the right panel, closely tracks the as-polished surface figures of the individual segments, as measured during ground testing years ago, shown in the left panel. JWST's wavefront sensing and mirror control systems are working as intended, achieving optimal alignments within the ~10 nm resolution of the sensing and control system and correcting as necessary to maintain that alignment. Data from PID 1163.*

4.2 Comparison to optical budget for the telescope and science instruments

JWST has top-level science requirements to achieve image quality with Strehl ratio greater than 0.8 in NIRCam at a wavelength of 2 μm (equivalent to wavefront error of 150 nm rms) and MIRI at a wavelength of 5.6 μm (equivalent to 420 nm rms). These and other top-level requirements flowed into detailed optical performance budgets and lower-level requirements, such as a required telescope wavefront error ≤ 131 nm rms over the fields of view of the science instruments, a required telescope stability of ≤ 54 nm rms over two weeks, and so on. Though line-of-sight image jitter is distinct from WFE, it is also tracked within the same budget via a computed equivalent WFE.

Figure 4 presents an abbreviated summary comparing measured performance in flight to those budgets at high level. Note that the measured values shown here are from commissioning at observatory "beginning of life", while the required and predicted values were derived for "end of life" after a notional 5-year mission. At the observatory top level, the achieved WFE is well below predictions by ~30%, and the remaining performance margin relative to requirements is large. All lower-level terms are at or below requirements values, with the sole exception of the high frequency WFE which was increased by the May 2022 micrometeoroid impact. Terms with particularly notable performance relative to requirements include the telescope stability (see section 4.5), the line of sight pointing (section 3.3), and the wavefront quality of the science instruments (which are all significantly better than their requirements).

An initial assessment, which combined the measured beginning-of-life performance with model predictions for observatory aging in the L2 environment, predicts that JWST should meet its optical performance requirements for many years. The current largest source of uncertainty in models is the rate

of mirror surface degradation from micrometeoroids, discussed below.

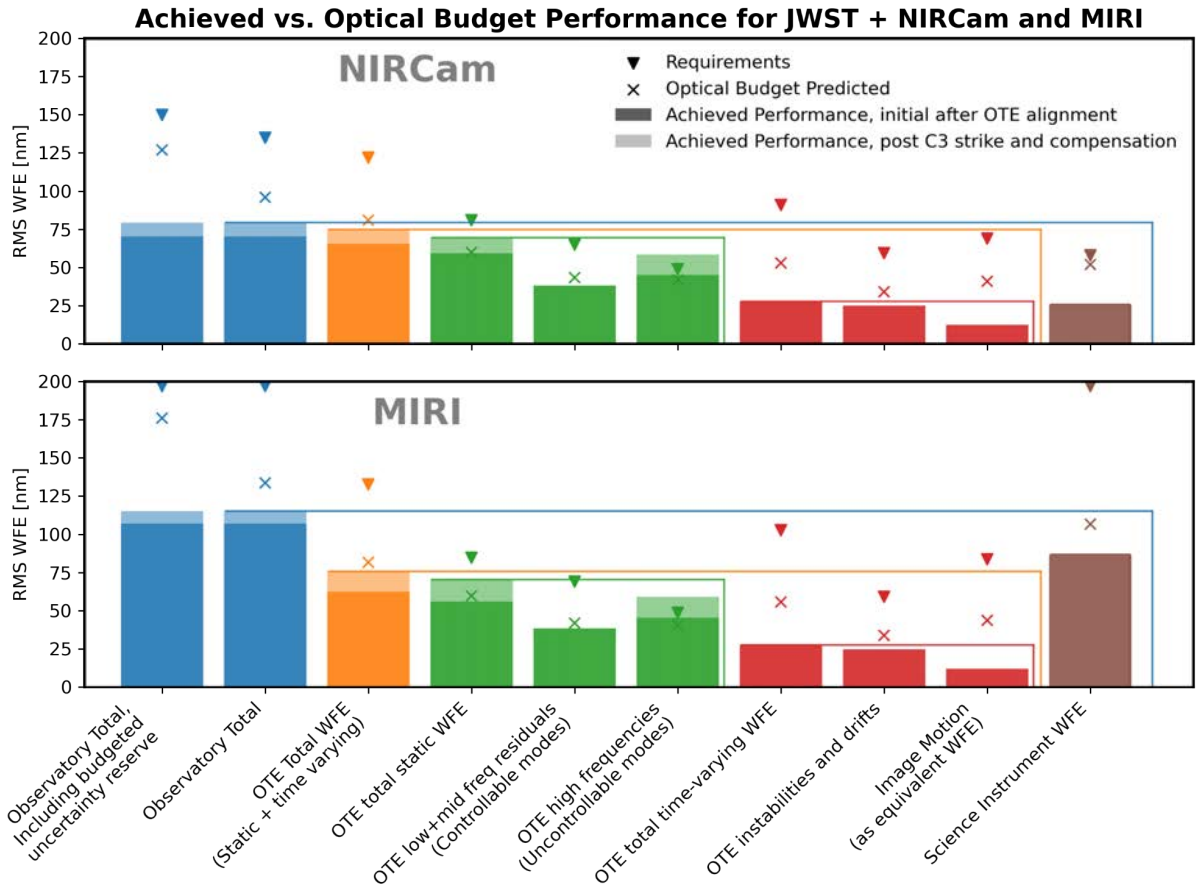

Figure 4: High-level summary representation of JWST optical performance for 2.0 and 5.6 µm. *For each contribution to wavefront error, triangles represent the required level, Xs mark the pre-launch optical budget predicted levels, and bars indicate the measured performance. All Optical Telescope Element (OTE) values shown are from on-orbit measurements. Science instrument WFE values shown are for typical field points (median SI image quality) in NIRCam and MIRI, as measured on the ground during ISIM CV3 testing. The colored lines depict which terms sum together; for instance the OTE total WFE is the RSS sum of the OTE static WFE and OTE time-varying WFE. Shaded portions of the bars indicate the delta in performance from the May 2022 micrometeoroid strike on segment C3.*

4.3 Shape of the point spread function

JWST's hexagonal aperture creates a characteristic diffraction pattern in its point spread functions, with six stronger diffraction spikes at 60 degree intervals created by the segment and aperture edges, plus two fainter horizontal spikes created by the vertical secondary mirror support. While these diffraction spikes can be visually dramatic in images which are deeply exposed or are plotted with log stretches, it is the case that the majority of light is focused into the PSF core (typically ~66% within the first Airy ring).

Compared to the diffraction patterns from circular apertures which many astronomers are more familiar with, such as Hubble, the hexagonal geometry of JWST concentrates wide-angle diffracted light more strongly into the diffraction spikes, while the areas between those spikes are relatively darker. For bright

sources the diffraction spikes can be seen to a separation of many arc minutes, falling off as ~ $R^{-1.5}$, including diffraction spikes from sources outside of an instrument's field of view.

Note that the position angles of the six bright diffraction features are different between the PSF core region (2-5 λ/D, dominated by diffraction from the overall outer hexagonal outline) and the outer wings (>5 λ/D, dominated by diffraction from the individual segments). See Figure 2. This can be understood intuitively from the pupil geometry: when assembling a larger hexagon from smaller hexagons, the outline of the larger hexagon which is created is rotated 30 deg relative to the smaller ones.

Additional PSF details per instrument:

- MIRI imager and MRS PSFs, particularly at wavelengths ≤ 10 μm, show additional diffraction spikes in vertical and horizontal directions in the instrument coordinate frame, called the "cruciform" or "cross artifact". These arise due to diffraction that occurs internal to the detector at the detector electrical contacts. This effect was seen in Spitzer's similar Si:As detectors, and was modeled and expected for MIRI (Gaspar et al. 2020). Improved models based on flight data are able to reproduce this artifact in detail including the field dependence. Pipeline steps are being developed to compensate for its impact on MIRI MRS data cubes.
- NIRISS imaging PSFs at wavelengths ≥ 2.7 μm have stronger diffraction spikes due to additional pupil obscuration from the CLEARP pupil wheel position which must be used with those filters.
- NIRISS imager PSFs at wavelengths ≤ 2.0 μm show additional anomalous or "extra" diffraction spikes, which are more diffuse than the ordinary spikes and have a position angle that varies strongly with field position. The intensity of the anomalous spikes decreases with wavelength, in F090W containing ~70% of the flux of the normal vertical diffraction spike, becoming barely detectable by F200W. These spikes are now understood as due to diamond-turning tool marks on off-axis mirrors within NIRISS. Retroactive examination of some ground test data also shows their presence at lower SNR. A similar effect is also seen in FGS PSFs.
- The rotation of NIRSpec in the focal plane means that, in the detector coordinate system, NIRSpec PSFs are rotated by 139 deg relative to the other instruments. MIRI is similarly rotated 5 deg.
- Instrument modes with specialized optical components, such as NIRCam coronagraphy, MIRI coronagraphy, NIRISS aperture masking interferometry, and NIRISS SOSS, each have their own PSF properties, not described here. These observed PSFs are in general highly consistent with model predictions.

4.4 Transmission and contamination

The telescope's effective area, the product of the telescope area and its transmission, is a key optical performance parameter that was tracked through development and characterized on orbit. The JWST unobscured telescope area was required to be > 25 m^2. The measured value using the NIRCam pupil imaging lens was 25.44 m^2. The telescope's wavelength-dependent transmission ranged from 0.786 at 0.8 μm to 0.933 at 28 μm, better than requirements at each wavelength. Even though the JWST optics spent significantly more time in ground facilities than originally anticipated, these high transmissions were maintained with careful control of contamination throughout the integration and test phases and during preparation for launch. Brush cleaning was also carried out on the telescope primary mirror segments and secondary mirror to remove particulates.

4.5 Optical stability on different timescales

Commissioning observations characterized the telescope's optical stability and variations on multiple timescales. Highly precise wavefront sensing allows measurement of very small changes (<10 nm). The overall amplitudes of variation are close to predicted values, however some timescales are faster than expected. These variations have small but measurable effects on PSF properties, which should be taken into account for measurements at the highest precision, but will be negligible for many science cases (similar to the effect of the "breathing" variations seen in Hubble PSFs on orbital timescales).

Overall stability: During the last month of commissioning, 2022 June, the change in wavefront measured between successive observations roughly 2 days apart was typically ≤ 25 nm rms, and frequently less than half that (range 8–50 nm rms per 2 days). During this time period, the observatory was conducting a wide range of commissioning and Early Release Observations typical of science activities, so this level of stability should be representative of what can be expected during Cycle 1.

Though we provide details below on observed variations over time, we wish to emphasize that these are *small* variations. The absolute amplitude of drifts seen between successive wavefront monitoring visits is comparable to the Hubble Space Telescope's ~18 nm rms of focus variation typical on orbital timescales (see e.g. Lallo 2012). Yet for JWST the variations are observed to mostly occur on significantly longer timescales, and the effect on images at longer wavelengths is correspondingly reduced. (Hubble is typically stable to $\lambda/30$ at λ=0.5 μm over 90 minutes; JWST is often stable to $\lambda/100$ at λ=2 μm over 2 days.) Also similar to Hubble, the amplitude of wavefront variations over time is comparable to and generally less than the field-dependent variations within a given instrument.

Factors contributing to stability levels: The telescope is very thermally stable, but small changes in equilibrium temperature (< 0.1 K, within the temperature sensor noise) can still occur in response to changes in attitude with respect to the sun. Variations from instrument heat sources can also affect telescope structures. A thermal stability exercise measured these effects by moving between the extremes of JWST's field of view, with a week-long soak at "cold" attitude (-40º pitch relative to the sun) sandwiched between an equal amount of time at the "hot" attitude (0º pitch); this test is intentionally more stressing than typical attitude profiles during science operations. The thermal slew exercise (PIDs 1445, 1446) included a wide range of wavefront sensing, imaging, and sensor telemetry investigations to characterize many aspects of JWST's performance on multiple timescales. Modes of variation observed with JWST include the following.

4.5.1 Telescope backplane thermal distortion: After backing out the contributions from tilt events (see below), the observed drift in wavefront during the thermal slew test could be well fit as a double exponential. The largest and slowest term arises from thermal deformation of the observatory backplane in response to the small change in equilibrium temperature. In the thermal slew test this was measured to be ~18 nm with a time constant of 1.5–2 days. In comparison the preflight prediction from integrated modeling was 14.6 nm with a time constant of 5–6 days predicted at observatory beginning of life, versus requirements of 54 nm rms. The dominant mode in this drift is zero-degree astigmatism, essentially a bending mode of the primary outer segment "wings" relative to the center section, in accordance with predictions.

4.5.2 Telescope soft structure thermal distortion: The second term in the double exponential fit represents wavefront drift which arises from soft structures. The black Kapton stray-light-blocking "frill" around the outside of the primary can place mechanical stress on its points of attachment when it thermally expands and contracts. The lower thermal mass of the frill causes this to have a shorter characteristic timescale. The observed effect in the thermal slew test

was an exponential with 4.45 nm amplitude and time constant of 0.77 hours immediately after the slew from hot to cold attitude[6]. In comparison, the preflight prediction was 8.6 nm with a time constant of 8–10 hours.

4.5.3 Fast oscillations from heaters: On short timescales (2-4 minutes), the thermal cycling of heaters in the ISIM Electronics Compartment (IEC) induces small forces on the telescope backplane structure. The observed result is a semi-periodic variation primarily in astigmatism with amplitude of about 2.5 nm, which is closely consistent with preflight predictions. The exact amplitude and timescale vary as the cycles of several different heaters beat together. This oscillation is sufficiently small and rapid that it has thus far only been measured in special high-cadence differential wavefront sensing measurements which achieve sub-nanometer precision. This effect is expected to be negligible for the vast majority of science observations.

4.5.4 Segment tilt events and other drifts: "Tilt events" are occasional abrupt changes in position of an individual segment which are seen to occur from time to time, with varying amplitudes of a few nanometers to tens of nanometers. These are hypothesized to be due to structural microdynamics within the telescope (e.g. localized relaxations of stiction or micro-stresses within the backplane structure). This hypothesis is supported by a few cases in which measurable stress relief was detected by telescope wing latch strain sensors at the time of tilt events. Fast wavefront sensing measurements constrain the time scale for some tilt events to be < 10 s; these are effectively instantaneous step functions in mirror position.

Since a few such events were first seen during the OTIS cryovacuum testing on the ground, it was expected these might be seen in flight, particularly initially after cooldown. Tilt events have proven to be not infrequent, though the rate may be decreasing over time: During April–May 2022 there were periods in which small tilt events occurred as frequently as two to three per day, but by later June 2022 there were weeks with few or no tilt events. The expectation that tilt events would be small and would stabilize as the micro-stresses are relieved seems to be in line with the reduction we are seeing and the fact that they are small.

Tilt events may cause small but observable changes in PSFs during some science observations. The resulting change to encircled energy is very small (small fractions of a percent) and much smaller than encircled energy stability requirements. However it can be significant for observations at very high precision. For instance tilt events were observed in the NIRCam and NIRISS time series commissioning tests, and caused abrupt small step-function offsets in the initial measured flux analysis (for example, see Section 6.1.2). Flux jumps caused by occasional tilt events can be calibrated as a function of aperture size or wavelength and/or be included as a parameter in the transit fit model. The time sequence of FGS image data and centroids obtained at 15.6 Hz during all science observations may also be a useful diagnostic channel for some tilt events.

Not all changes in segment position occur on the rapid timescale of tilt events; at times, slow drifts of segment positions over hours or days have been observed as well. Understanding of the

[6] While one might assume the amplitude of this effect to be independent of slew direction, this was not observed to be the case: after the reverse slew from cold to hot attitude, a similar exponential drift was not seen, and instead the wavefront was stable to within 3 nm over the 6 hour measurement period. Due to test duration it was not possible to repeat these measurements for further investigation of under what circumstances the frill term does or does not manifest.

structural dynamics of this segmented telescope in space will continue to improve with time.

4.6 Routine Wavefront Sensing and Control

Since the completion of telescope alignment, regular wavefront sensing and control has monitored and maintained telescope alignment, as will continue throughout the mission. During science operations, wavefront sensing measurements are being planned every 2 days (roughly, with flexible cadence around science observations). The resulting measurements of mirror alignment state versus time are automatically made available in the MAST archive; software for making use of these measurements to produce time-dependent PSF models is now included in the WebbPSF package.

The telescope wavefront error at which a realignment will normally be performed is currently ~80 nm rms. Typical wavefront error over the last several weeks has been generally between 65 and 75 nm rms for the telescope alone, with corrections occurring about once per week or two.

Because of the 2-day cadence of wavefront sensing measurements, wavefront states at times between those measurements are not directly measured (e.g. if a tilt event or micrometeoroid impact occurs within some 2 days, its exact time of occurrence is not measured). Some science modes do allow for more frequent wavefront measurements, in particular NIRCam time series using the weak lens in the short wave channel, and to some extent the NIRISS SOSS mode.

4.7 Micrometeoroids

Inevitably, any spacecraft will encounter micrometeoroids. During commissioning, wavefront sensing recorded six localized surface deformations on the primary mirror that are attributed to impact by micrometeoroids. These occurred at a rate (roughly one per month) consistent with pre-launch expectations. Each micrometeoroid caused degradation in the wavefront of the impacted mirror segment, as measured during regular wavefront sensing. Some of the resulting wavefront degradation is correctable through regular wavefront control; some of it comprises high spatial frequency terms that cannot be corrected. There should also be a small effect on the telescope throughput, which is not yet measurable. Of the six micrometeoroid strikes detected thus far through wavefront sensing, five had negligible effects, contributing a combined total of < 1 nm to the overall wavefront error.

By contrast, the micrometeoroid which hit segment C3 in the period 22—24 May 2022 UT caused significant uncorrectable change in the overall figure of that segment. However, the effect was small at the full telescope level because only a small portion of the telescope area was affected. After two subsequent realignment steps, the telescope was aligned to a minimum of 59 nm rms, which is about 5-10 nm rms above the previous best wavefront error rms values[7]. It should be noted that the drifts and stability levels of the telescope mean that science observations will typically see telescope contribution between 60 nm rms (minimum) and 80 nm rms (where WF control will typically be performed). Further, the telescope WFE combines with the science instrument WFE to yield total observatory levels in the range 70-130 nm (see Table 2), so the slight increase to telescope WFE from this strike has a relatively smaller effect on total observatory WFE.

Imaging of the primary using the NIRCam pupil imaging lens is sensitive to changes from smaller

[7] The impact raised the wavefront error of segment C3 from 56 to 280 nm rms. Mirror commanding to adjust segment position and curvature reduced this error to 178 nm rms. This, after dividing by area and adding in quadrature to the other sources of WFE in the telescope, results in ~9 nm rms increase to the total telescope wavefront error.

impacts, below the threshold to be detectable by wavefront sensing. Comparison of pupil images taken 23 Feb and 26 May 2022 show evidence for 19 such minor strikes over that 92 day period. Regular monitoring of the pupil may help constrain the micrometeoroid hit rate and power spectrum.

It is not yet clear whether the May 2022 hit to segment C3 was a rare event (i.e. an unlucky early strike by a high kinetic energy micrometeoroid that statistically might occur only once in several years), or whether the telescope may be more susceptible to damage by micrometeoroids than pre-launch modeling predicted. The project team is conducting additional investigations into the micrometeoroid population, how impacts affect beryllium mirrors, and the efficacy and efficiency tradeoffs of potential mitigations such as pointing restrictions that would minimize time spent looking in the direction of orbital motion, which statistically has higher micrometeoroid rates and energies.

5.0 Backgrounds, stray light, and scattered light

The level of background emission is critical to the depth of many JWST imaging and low-spectral-resolution spectroscopic observations. Two major components of the backgrounds — the near-infrared stray light and the mid-infrared thermal self-emission — before launch could only be estimated with large uncertainties (~20% and ~50%, respectively). Estimated background levels were included in the JWST proposal tools, and will be updated to as-measured values in time for the Cycle 2 Call for Proposals. Here, we describe the actual strengths of these backgrounds.

5.1 Near-infrared stray light

In the near-infrared, JWST detects not only the "in-field" backgrounds from our Solar System and our Galaxy in the direction the telescope is pointed, but also "stray light" that creeps into the unbaffled telescope from other sight-lines. The amount of stray light was fairly uncertain before launch, as it depends on the amount of dust contamination on the mirrors. In commissioning we measured this stray light emission in multiple deep fields, in program 1448.

Figure 5 shows the results for the benchmark field, the "1.2 min zodi field", which was chosen to be a particularly challenging case for stray light, and where the near-infrared background is 1.2 times its lowest value on the sky. The observed points (dots and blue line) are consistently at or less than the model predictions (thick dashed black line). This commissioning activity demonstrated that JWST meets its near-infrared stray light requirements in the benchmark field. The backgrounds were even lower in fields that were predicted to have very low backgrounds, such as the Extended Groth Strip and the South ecliptic pole.

Taken together, the results from this program demonstrate that for deep fields, JWST will have less near-IR stray light than expected, meaning that deep fields at high ecliptic latitude will go deeper faster than expected.

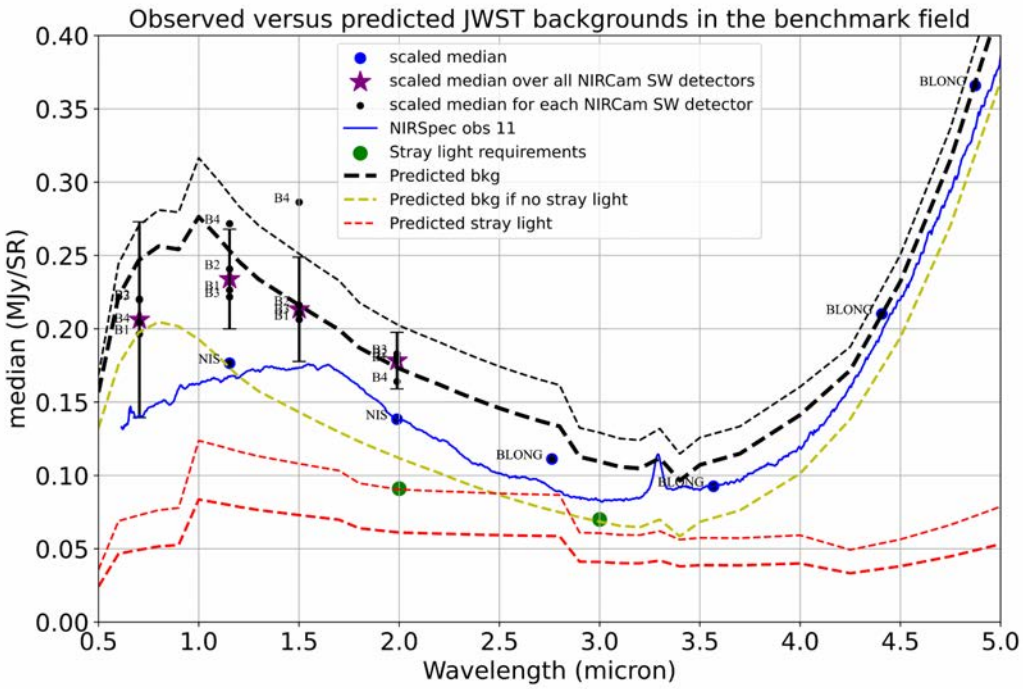

Figure 5: The observed levels of near-infrared background in the benchmark "1.2 min zodi" field. *Purple stars show the observed median level over all NIRCam short-wavelength detectors. The small black dots show the median level for each NIRCam short-wavelength detector. Blue labeled dots show the median level in NIRISS (labeled "NIS") and NIRCam long-wavelength (labeled "BLONG"). The blue curve shows the spectrum extracted from a selected NIRSpec MOS shutter. Dashed lines show the predicted backgrounds for this field on the day it was observed, from the JWST Background Tool, separated into components (red for stray light, yellow for in-field, total in black). The thin dashed lines show how much the expected stray light component of the background would need to be scaled up, to match the stray light requirements values (green circles). Despite offsets in the background levels among the three near-IR science instruments that merit further investigation, the result is clear that the observed total background levels are at or below the pre-launch expectations, and much less than the requirements. The near-infrared sky that JWST sees will be darker than expected, which should make the observatory more sensitive than pre-launch predictions. Data from program PID 1448.*

5.2 Mid-infrared thermal self-emission

In the mid-infrared, the background is dominated by a combination of scattered thermal emission from the sunshield and other parts of the spacecraft, and thermal emission from the primary mirror. Figure 6 shows the measured backgrounds in the long-wavelength MIRI broad-band filters during commissioning. The background levels are remarkably constant with time, and do not seem to correlate significantly with sun pitch angle as was expected before launch.

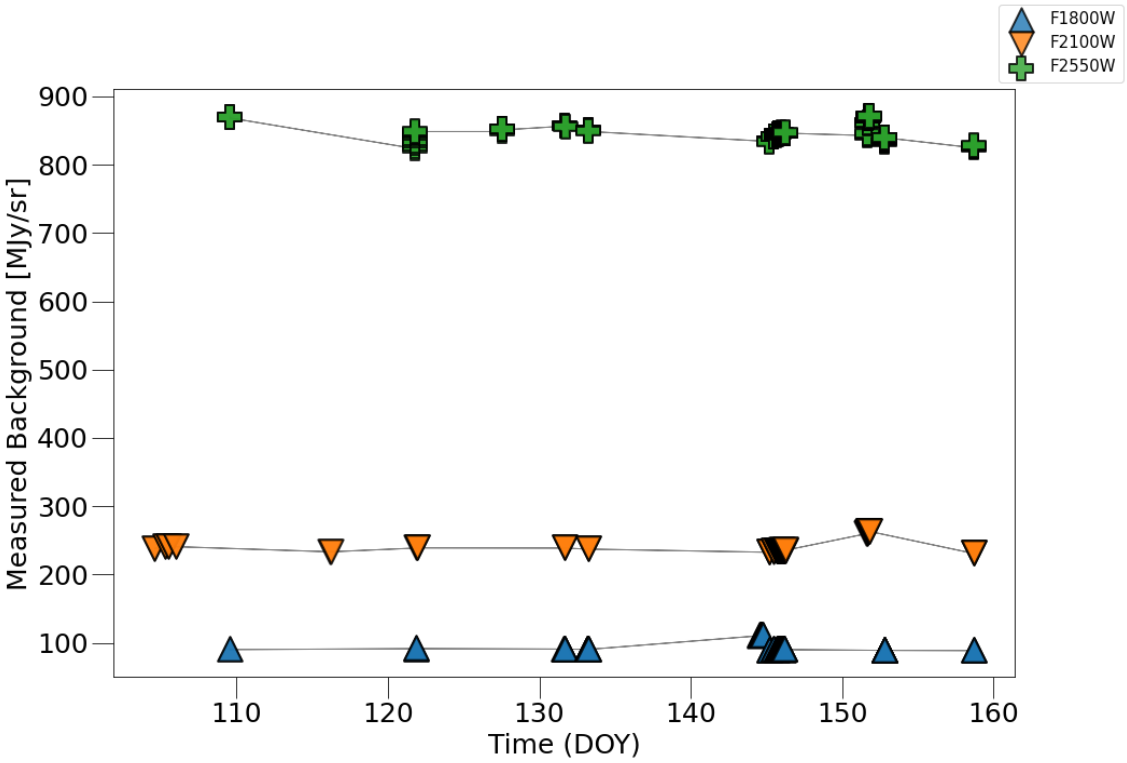

Figure 6: Mid-infrared background levels and their variability with time. *Plotted are backgrounds measured from MIRI imaging at 18, 21, and 25 μm in the F1800W, F2100W, and F2550W broadband filters, respectively, taken over the span of commissioning where MIRI was at operating temperature. At these long wavelengths, scattered thermal emission from the sunshield and thermal self-emission from the primary mirror dominate over astrophysical backgrounds.*

Figure 7 shows the spectrum of the mid-IR background, using the same data as Figure 6. This background was considered to be uncertain at the 30–50% level before launch, as it depends on the final temperatures of the primary mirror, as well as the deployed shape and scattering properties of the sunshield. Nevertheless, the pre-launch curve describes the measured backgrounds remarkably well. For reference, the requirement was an equivalent background of 200 MJy/sr at 20.0 μm; given these measurements, that requirement is met.

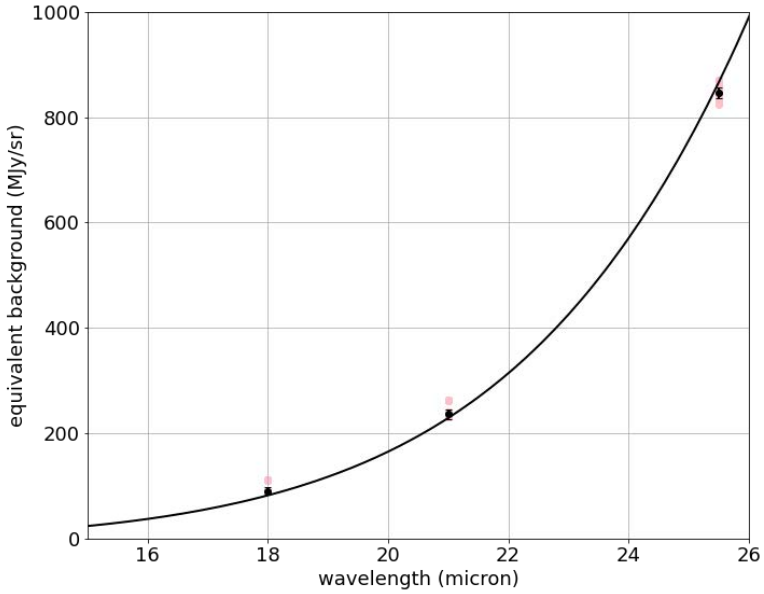

Figure 7: Spectrum of the mid-infrared background seen by JWST. *The data from the previous figure are plotted as pink circles; black circles plot the median and standard deviation of those data for each wavelength. The black curve is not a fit — instead, it is the pre-launch estimated mid-infrared background spectrum that is currently used by the exposure time calculator and the JWST background tool, which in turn was derived from detailed integrated models of the observatory.*

5.3 Scattered light features from the rogue path

During commissioning, a few unexpected stray light features were discovered, characterized and understood, and mitigation plans developed.

There exists a stray light path, termed the 'rogue path', that bypasses the primary and secondary mirrors, directly passes through the aft optics system (AOS) aperture just over the back of the fine steering mirror, and reaches the science instrument pick off mirrors (Lightsey et al., 2014). While the rogue path was anticipated, and steps taken to block it to the extent possible, the NIRCam and NIRSS instruments at times show some unexpected scattered light features which have been identified as being due to this path. Different effects arise, termed "wisps", "claws" in NIRCam and "the lightsaber" in NIRISS. These features are relatively faint, but for some observations such as deep fields these could be significant noise terms if not mitigated. Their properties are discussed further below in the science instrument sections, and more information may be found at the JDox Data Features and Image Artifacts page.

Stray light modeling associated the claws and lightsaber with the presence of bright (0—1st Vega mag) stars in the "rogue path" susceptibility zone: a region of the field of view located several degrees off the telescope boresight (10 degrees for NIRCam, 13 degrees for NIRISS). Light from bright stars in this zone can bypass the telescope optical train, enter the SIs through the SI pickoff mirrors, then bounce from non-optical surfaces within the science instruments to the detectors. During commissioning, we directly mapped the extent of the rogue path susceptibility zones for both NIRCam and NIRISS by moving a bright star through the susceptibility zone.

These features may be avoided simply by ensuring observations do not place very bright stars in this zone. Data processing steps to subtract out these features when present are also under development. During Cycle 1, STScI will continue to analyze the prevalence and strength of claws and the lightsaber as they appear in NIRCam and NIRISS datasets. STScI plans to update the Astronomers' Proposal Tool to alert users when planned observations would place bright stars in the susceptibility zone, to give users advance predictions of the artifacts and allow replanning observations to avoid them.

The "wisp" features in NIRCam arise from a different optical path, stray light that reflects from the upper strut which supports the secondary mirror. These are fixed in position and expected to subtract out well.

6.0 Science instrument performance

JWST has 17 science instrument modes. Near the end of commissioning, the science performance of each mode in turn was reviewed against criteria developed pre-launch for such parameters as sensitivity, image quality, wavelength calibration, astrometric calibration, ghosts, stability, and so on. As of 10 July 2022, all 17 of the 17 modes have been approved to begin science operations. With the performance of the instruments being uniformly excellent vs. requirements and typically also better than pre-flight estimates, the assessments of modes as being ready for Cycle 1 science have been quite straightforward. Below we summarize the performance and any known issues for each instrument mode.

A key result of science instrument commissioning is that overall, the JWST science instruments have substantially better sensitivity than was predicted pre-launch. This result is due to higher science instrument throughput, sharper point spread functions, cleaner mirrors, and lower levels of near-infrared stray light background compared to pre-launch expectations. The exposure time calculator (ETC) and JWST user documentation (JDox) will be overhauled to reflect on-orbit performance, in time to support the Cycle 2 Call for Proposals. Once updated, the ETC and JDox will be the definitive reference as to sensitivity. For now, we quote several representative measurements and calculations that were determined during commissioning.

Across all instruments, JWST has multiple time series observation (TSO) modes to support observations of transiting exoplanets. During commissioning, observations of the exoplanet HAT-P-14 b were obtained with three NIR spectroscopic modes—the NIRCam grism time series mode, the NIRISS SOSS mode, and the NIRSpec BOTS mode—to enable cross-comparison between instruments and assessment of astrophysical versus instrumental systematics. This target was chosen because, as a massive planet with a high surface gravity, it is expected to have a flat transmission spectrum. It also has a relatively bright host star ($K_{s,\ Vega}$=8.9). In addition the transiting exoplanet L 168-9 b was observed with the MIRI LRS time series mode. Results are given in the subsections below for each instrument; the overall picture is that JWST is returning precise transit spectra with minimal processing.

Mode readiness reviews also included the documentation of any remaining work needed to enable particular use cases (e.g. nudging a subarray location slightly to not clip a spectrum; updating an astrometric file needed for Target Acquisition) or the identification of performance features that observers should be made aware of before final planning of their observations (e.g. alerts regarding faster-than-expected saturation due to higher-than-expected throughput, or warnings regarding stray light features such as the "claws" and "lightsaber", with tips for mitigation). These issues are captured as "liens" on the mode readiness that must be addressed for some specific observing programs (or that will be addressed by the operations team in the near term as "normal work"). Observations not affected by liens are ready for immediate insertion into the observing plan. Following the first several mode readiness

reviews, cycle 1 observations of early release science targets began on 20 June 2022. GO and GTO cycle 1 programs have followed.

6.1 NIRCam performance

6.1.1 NIRCam imaging

The throughput of NIRCam meets or slightly exceeds pre-launch expectations for all but a few of the filters in the short wavelength channel. In the long wavelength channel, the throughput is systematically 20% higher than expected for most filters. Figure 8 shows the throughput of NIRCam compared to what was assumed in the pre-launch version of the ETC.

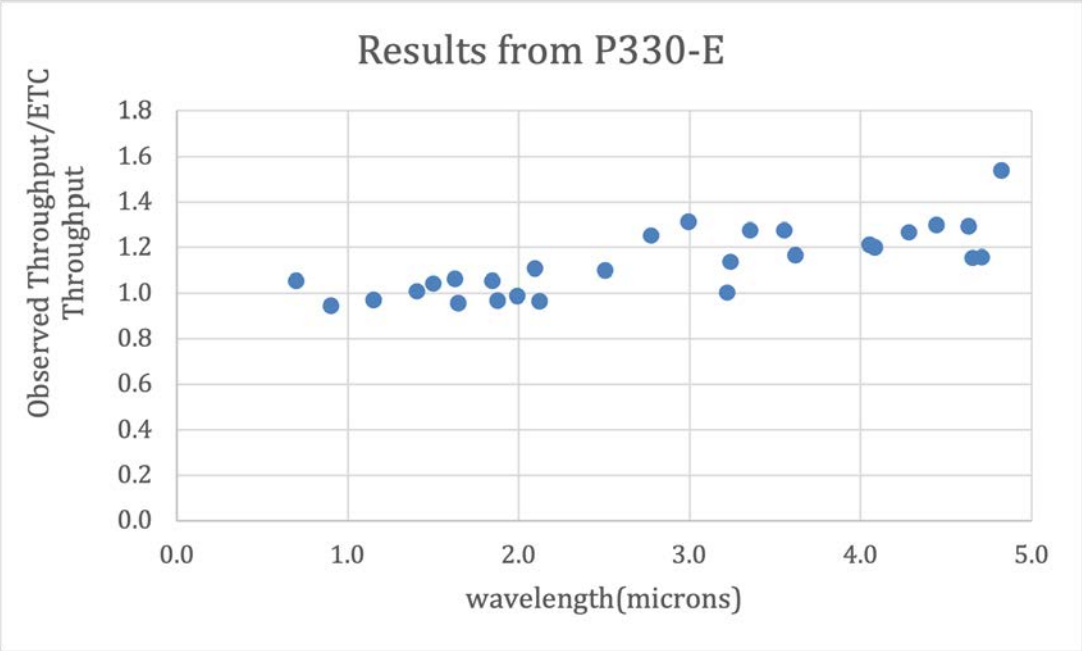

Figure 8: NIRCam imaging throughput compared to what was assumed in the pre-launch ETC. *For most filters, the observed throughput is higher than the pre-launch expectations. Data are from spectrophotometric standard star P330-E observed in program PID 1074.*

The point spread function is better than expected, as parameterized by encircled energy or full width at half maximum. The photometric stability is stable to at least 4%, and is likely much better. The residual astrometric errors are 2–4 milliarcseconds per filter across a detector. Optical ghosts are consistent with expectations from ground tests. Some scattered light features are seen (the “claws” and “wisps”, described below), which may have some impact on deep imaging.

Table 3 compares the required, predicted, and on-orbit limiting point-source sensitivity of NIRCam imaging. The limiting sensitivity is the faintest point source that can be detected at signal to noise ratio SNR=10 in an integration time of 10,000s. For a representative wavelength for each of the short and long-wavelength channels, the table quotes the requirements values, the pre-launch predictions from the exposure time calculator, and the predicted performance assuming the measured on-orbit throughput, PSF, and detector noise levels. This is predicted performance, not measured performance, as commissioning in general did not involve long integrations. Table 3 predicts that NIRCam imaging should detect faint

objects substantially faster than pre-launch expectations.

We quickly compare this limiting point source sensitivity to Hubble and Spitzer, again considering the faintest point source detectable at SNR=10 in 10,000s, For NIRCam at 1.5 μm, the sensitivity is 6 times better than WFC3-IR on Hubble. For NIRCam at 3.5 μm, it is 68 times better than IRAC on Spitzer. The integration time required to achieve a given limiting sensitivity, relative to these previous instruments, scales roughly as the square of these advantage factors for the common case of background-limited broadband imaging.

Wavelength (μm)	**2**	**3.5**
Requirement (nJy)	11.4	13.8
ETC prediction (nJy)	10	14.1
Actual (nJy)	7.3	8.8

Table 3: NIRCam limiting point source sensitivity. *What is quoted is the faintest flux density that can be detected at SNR=10 in 10,000s. Values are for wide-band filters. Smaller numbers are better.*

Filter	**Throughput (DN/sec/nJy)**	**Sensitivity (nJy)**
F070W	0.0088	14
F090W	0.0116	11
F115W	0.0132	9.6
F140M	0.0081	13
F150W	0.0177	7.9
F162M	0.0085	13
F164N	0.0009	82
F182M	0.0115	10.
F187N	0.0010	79
F200W	0.0197	7.3
F210M	0.0093	13
F212N	0.0011	78
F250M	0.0066	24
F277W	0.0254	10
F300M	0.0112	16
F323N	0.0010	102
F335M	0.0126	14
F356W	0.0288	8.8
F360M	0.0123	15
F405N	0.0012	92
F410M	0.0132	18
F430M	0.0068	33
F444W	0.0320	16

F460M	0.0056	54
F466N	0.0009	170
F470N	0.0008	200
F480M	0.0078	52

Table 4: Preliminary throughput calibration factors and limiting point source sensitivities for all NIRCam imaging filters. *Calibrations are for detectors B1 and B5, and are in units of digital numbers per second per nanoJansky. Sensitivity values are in units of nanoJansky, and are for SNR=10 detections in 10,000s using a 2.5-pixel radius aperture against a sky background that is 1.2x the minimum zodiacal light brightness.. Smaller limiting sensitivities are better.*

6.1.2 NIRCam grism time-series

Observations of exoplanet HAT-P-14 b taken during commissioning demonstrated that the grism time series spectroscopy is working well. The NIRCam observations of HAT-P-14 spanned 6 hours, using the F322W2 filter and grism, as part of PID 1442. With simple detrending, the standard deviation of the transit spectrum (as fit by a limb darkened transit model) was 91 ppm at R=100, compared to the expected photon noise of 55 ppm. The settling time was observed to be 11 min for the short wavelength channel, and only an upper limit of 4 minutes for the long wavelength channel, with an upper limit of the amplitude of the settling of 150 ppm. The throughput for NIRCam grism spectroscopy is 20—40% higher than expected for most wavelengths. Users should be wary of saturation, particularly at long wavelengths.

Figure 9 and Figure 10 from the time series observation illustrate the utility of monitoring the star in NIRCam's short wavelength channel. Primary mirror segments are subject to small, spontaneous tilts (see Section 4.5.4), which are readily seen in the short wavelength images and which cause jumps in the grism data. The magnitude of the jump from the main tilt event at the center of the transit varies from 200 ppm to 1000 ppm depending on the wavelength and aperture size. As shown in Figure 8, a larger aperture size (16 pixels) will have a smaller jump magnitude than a smaller aperture size (8 pixels) but this can be at the expense of larger noise. For the short wavelength channel, the jump could essentially be eliminated beyond a 100 pixel radius. The jumps may be modeled as step functions as a free parameter when fitting the lightcurves and are essentially instantaneous in this case (less than the 1.4 second group time). The jump magnitude is strongly wavelength dependent so it is necessary to fit different jump magnitudes at different wavelengths.

The NIRCam grism commissioning test clearly meets performance requirements even with simple detrending, demonstrating that the NIRCam grism provides better performance than HST/WFC3 for stars of similar brightness. Additional detrending and analysis will presumably move even closer to the photon noise limit.

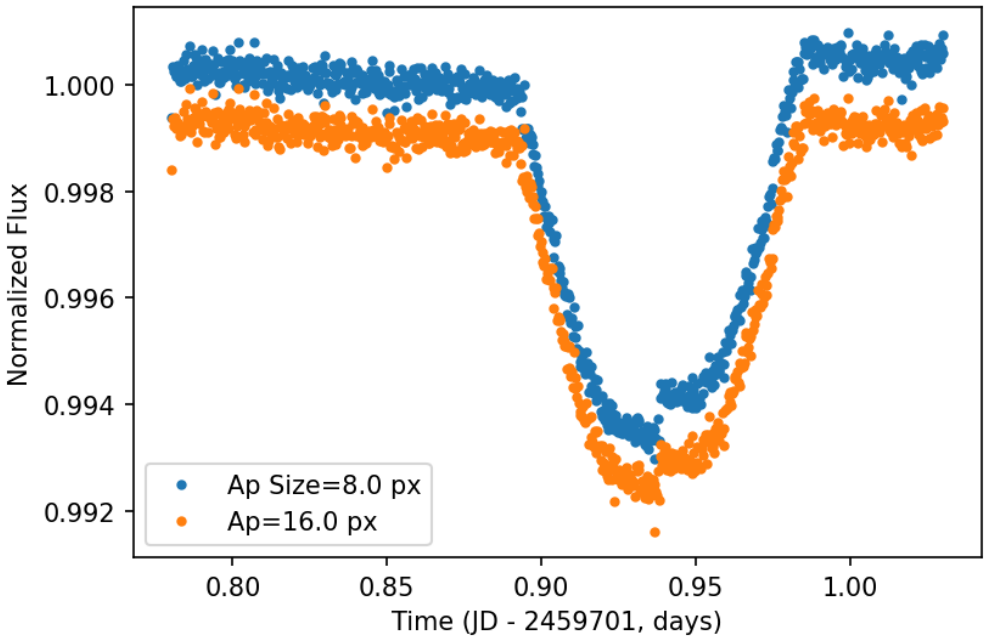

Figure 9: The summed broadband (2.4 µm to 4.0 µm) grism light curve from the HAT-P-14 observation. *The lightcurve from the NIRCam long wavelength channel shows excellent precision (195 ppm standard deviation out of transit) and no significant ramp systematics from charge trapping. For a smaller aperture size of 8 pixels (blue points), a larger jump (~600 ppm) was observed in the middle of the primary transit of the planet as well as a smaller one (~100 ppm) toward egress due to tilts in a primary mirror segment which occurred during the observation (see Section 4.5.4). The jumps magnitudes can be reduced with large aperture sizes (orange points). Data are from PID 1442.*

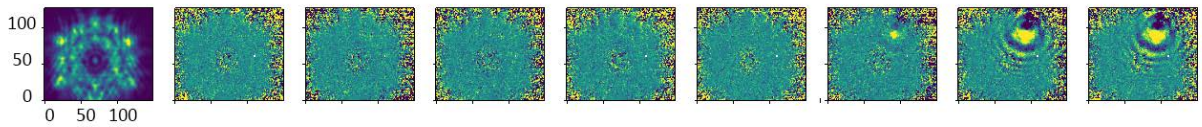

Figure 10: Weak lens data acquired at the same time as the light curve shown in Figure 9. *The weak lens image at the start of the time series is shown along with ratios of the images leading up to the tilt event. The tilted segment is very apparent, and the time of the appearance of the tilt coincides with the jump in the white-light curve.*

6.1.3 NIRCam photometric time-series

This mode is not heavily used in Cycle 1. In commissioning, the mode was checked out using a J_{Vega}=14 star with a short 500 s observation, in PID 1068. The performance was nominal: the standard deviation in the normalized flux was measured to be 0.62% (long wavelength channel) and 1% (short wavelength channel), both close to theoretical expectations.

6.1.4 NIRCam wide field slitless spectroscopy

NIRCam's Wide Field Slitless Spectroscopy (WFSS) has shown excellent performance through commissioning observations (PID 1076) of spectrophotometric and wavelength standards. Observations used the F322W2 and F444W filters to cover the full wavelength range of 2.5-5 μm. The full combinations of the two modules (A/B) and two grisms (R/C) were assessed for performance.

Observations of the spectrophotometric standard P330-E have shown that the total throughput of the NIRCam/WFSS mode is 20-40% higher than the pre-flight prediction for much of the 2.5-5 μm range and as much as 50-60% higher in the red end. This likely reflects our limited pre-flight understanding of the grism throughput and detector QE. This increased sensitivity is welcome news, but since it also lowers the saturation limits, observers targeting bright sources are advised to check their programs against the new limits. The P330-E data have also confirmed that the Mod-A total throughput is significantly higher than that of Mod-B (20-30% with F322W2 and 30-40% with F444W). This was expected because the Mod-A grisms are anti-reflection coated on both sides while the Mod-B ones are coated only on one side. Therefore, Mod-A is the preferred choice for NIRCam/WFSS observations (the throughputs of the R and C grisms are similar in both modules).

Wavelength calibration used IRAS 05248-7007, a post-AGB star in the Large Magellanic Cloud with bright emission lines. Analyses of those data confirmed that a stable and accurate wavelength calibration is possible (σ_{fit} = 0.2 pix = 1/10 resolution element, using a 3rd-order polynomial). The measured spectral dispersion is a few percent smaller than the 10 Å/pix assumed in the ETC. Although the difference is small, observers should note that the regions of full spectral coverage will become smaller because of the increased lengths of spectra.

In practice, the trickiest aspect for NIRCam/WFSS mode calibrations is the construction of accurate spectral trace models. Traces are not only tilted, but also change in direction of curvature from one side of the FOV to the other. The commissioning data were not enough to provide accurate trace models for all module/filter/grism combinations over the full FOV, so the pipeline processing may produce poor spectral extractions in some cases. However, spectral trace models will keep improving as we obtain more data through the Cycle-1 calibration program.

Observers should also pay attention to the existence of ghosts in the NIRCam/WFSS data that could mimic emission-line sources. These ghosts are produced by bright sources in the observed field, and mainly affect Mod-B data. Since the relation between the ghost and source positions has been well characterized, it is generally straightforward to decide whether a given feature is a ghost or real source.

Finally, in Figure 11 we illustrate the power of the NIRCam/WFSS mode by showing a serendipitous detection of a line-emitting galaxy at z=4.39 in the commissioning data. Note the strong detections of the [OIII] 5007 Å and Hα lines in the spectra, which securely identify the redshift of this galaxy.

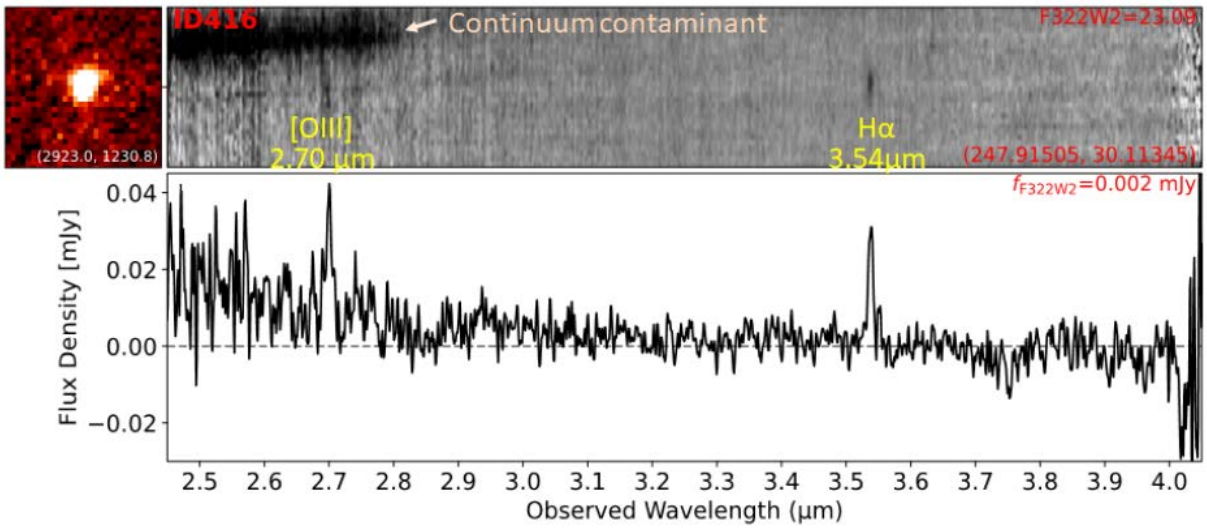

Figure 11: Spectrum of a z=4.39 emission-line galaxy. *This spectrum was detected serendipitously in 386 s of exposure time, in NIRCam wide field slitless spectroscopy mode data that targeted standard star P330-E for flux calibration, in PID 1076. Forbidden [O III] 5007 and H alpha are clearly detected.*

6.1.5 NIRCam coronagraphy

The performance of the NIRCam coronagraphs exceeds expectations. The NIRCam instrument has two short wavelength (SW) coronagraph masks (MASK210R and MASKSWB) and three long wavelength (LW) coronagraph masks (MASK335R, MASK430R, and MASKLWB). While each mask can be paired with a variety of filters, commissioning of the coronagraphs primarily focused on the nominal medium band filter for each mask. The commissioning process successfully demonstrated the contrast performance of all coronagraphs in their nominal filters.

To achieve science mode readiness for NIRCam coronagraphy, the NIRCam LW 335R mask with the F335M filter needed to demonstrate a 5-sigma PSF-subtracted contrast better than 10^{-4} at 1 arcsec. The contrast was directly measured during commissioning using multiple reference stars with and without small grid dithers (SGDs). The 335R contrast at 1 arcsec was consistently better than requirements, ranging from a value of ~4e-5 to ~4e-6, depending on TA repeatability and implementation of SGDs.

NIRCam coronagraphic TA is on par with requirements, achieving precisions ~0.5 pix 1-σ. The sidelobes of the coronagraphic PSF can contribute to increased centroid biases during TA; TA will continue to be an area of refinement during Cycle 1. However, in spite of these larger TA offsets, NIRCam contrast is excellent.

Figure 12 shows the range of azimuthally averaged PSF-subtracted contrasts measured for the 335R coronagraph with the 335M filter after a 3300 s exposure on a K=5.2 star. A nine-point small grid dither (SGD) was performed on the reference target. The light blue curves correspond to the worst case TA repeatability during commissioning, with each SGD position used as a unique reference star. The dotted blue curve shows the improved contrast when using all 9 SGDs with the KLIP algorithm. The dotted red line shows the contrast for the best case TA scenario with SGD and KLIP, and the dotted black shows the KLIP results with a larger PSF library. In scenarios with poor TA repeatability, SGDs combined with a PCA-style analysis can enhance contrast by a factor of ~10, while in scenarios of good TA repeatability the enhancement is a factor of ~2.

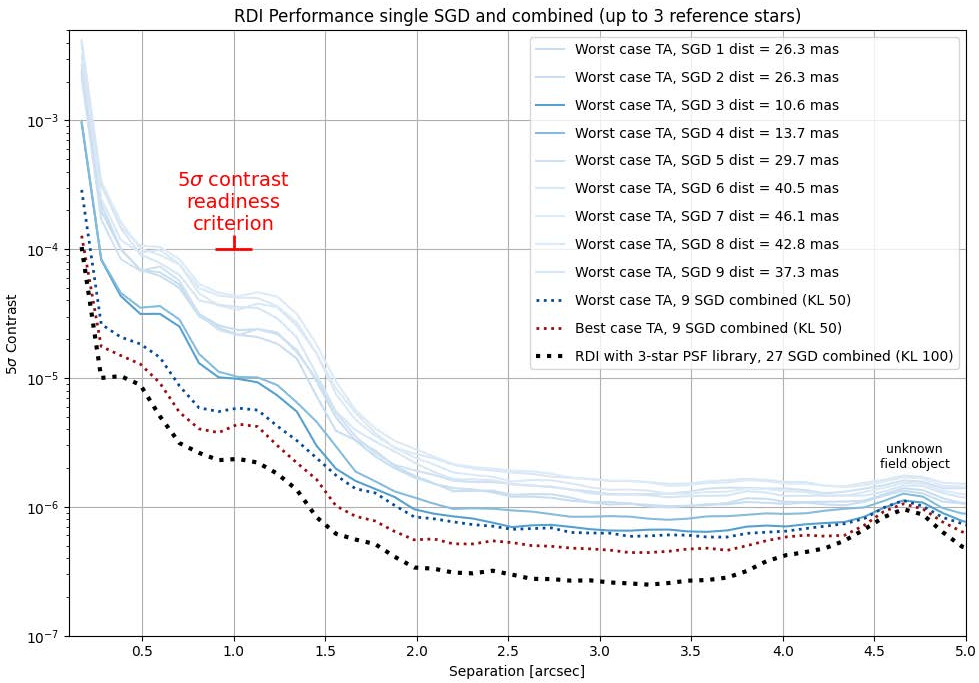

Figure 12: Contrast curve for NIRCam coronagraphy. *The range of PSF-subtracted contrasts measured for the 335R mask using the 335M filter. Blue curves show results using individual dithers/combined dithers on the PSF reference star for the* ***worst*** *case TA. The dotted red line shows the result using the PSF reference with the best TA, and the dotted black is the PSF-subtracted contrast via RDI with KLIP and a three star PSF library. The apparent bump in contrast at 4.6" is from the inclusion in the contrast curves of a source detected at that separation, plausibly a background galaxy. Data from PID 1441.*

Several stray light features have been identified in NIRCam imaging (see following sections). These features have not been observed in the NIRCam coronagraph fields of view; at this time there is no evidence that stray light will impact coronagraphy or that mitigation strategies need to be taken.

6.1.6 NIRCam stray light: Wisps, Claws, and other effects

Wisps: A few percent of the pixels in four of the eight NIRCam short wavelength detectors show small, faint, diffuse features that are termed "wisps". See Figure 13 and Figure 14. In the B4 detector wisps are always present, with variable brightness that is typically about 10% of the zodiacal background. Fainter wisps have also been seen in detectors A3, A4, and B3. Wisps occur at fixed detector positions. The origin of wisps has been traced to reflections from the upper strut that supports the secondary mirror. Since their detector positions are fixed, we expect that wisps can be well-subtracted from NIRCam short wavelength images. Wisps have not been seen in the NIRCam long wavelength channel.

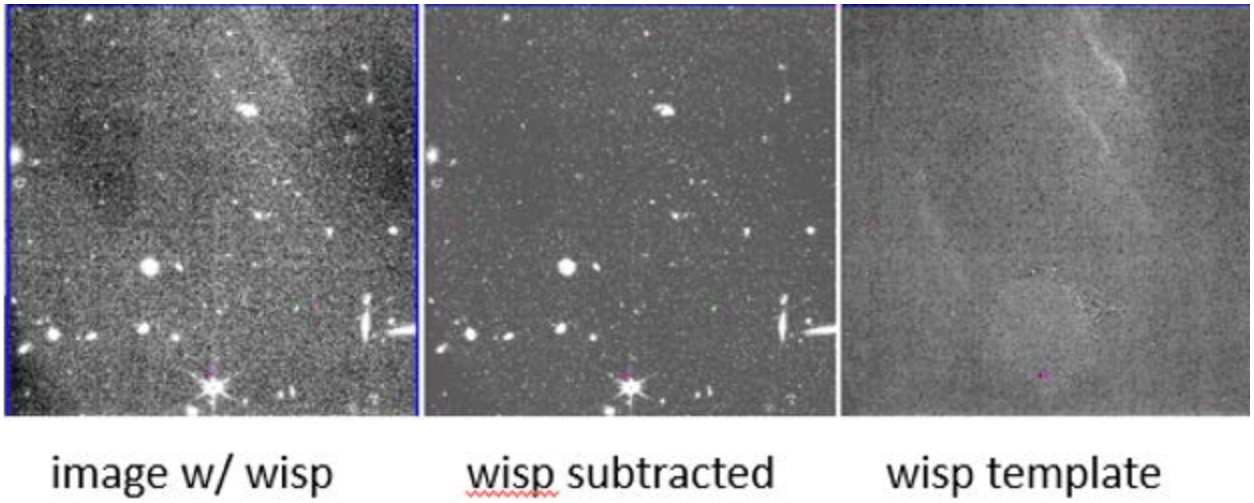

Figure 13: Wisps and their subtraction from NIRCam imaging data. *The left panel shows detector B4 with no correction. The middle panel shows the result of subtracting the wisp template, shown in the right panel, from the left panel.*

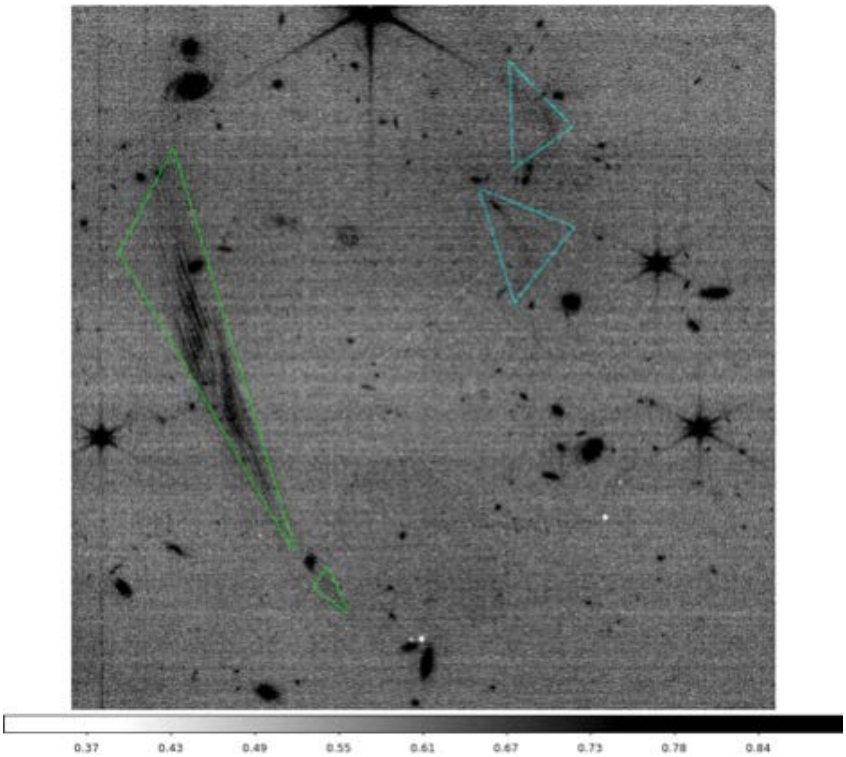

Figure 14: The NIRCam scattered light features "the claws" and "the wisps". *The claws are marked by green triangles, and the wisps by cyan triangles. Roughly 4% of the pixels in the detector B4 are involved in a claw, and 1.5% in a wisp. Data are from detector B4 of the NIRCam short wavelength channel. Of the 8 short-wavelength detectors in NIRCam, detector B4 is the one most affected by wisps, and one of the two most affected by claws. Data are from program PID 01063, in which bright star X Cancri (K=0.25 mag) was inside the claws susceptibility zone. Image used is jw01063142001_02101_00001_nrcb4_rateints.fits.*

Claws: A minority of NIRCam short wavelength channel images show "claws" – a faint diffuse pattern of scattered light features that moves across the detector coordinates as the telescope dithers. See Figure 14. Claws appear to be rare, but when present, have a brightness of about 10% of the zodiacal background. When present, claws occur primarily in the NRCA1 or NRCB4 detectors, affecting roughly 5% of the pixels on those detectors. Since claws move in detector coordinates, they are more difficult to subtract off than wisps. Claws arise when a bright star is located in the rogue path susceptibility region.

Other NIRCam stray light effects: Rarely, other scattered light artifacts have been seen in NIRCam images: Dragon's Breath (two types), Ginkgo Leaf, Tadpoles, and Shells, to date. All are described in the Data Features and Image Artifacts JDox page.

6.2 NIRISS performance

6.2.1 NIRISS imaging (parallel only)

The imaging performance of NIRISS matches or exceeds expectations. Shortward of 2 μm, the measured throughput is about 20% higher than the instrument team's expectations, and about 25–30% higher than the ETC's predictions. Longward of 2 μm, the throughput is about 5–10% better than the instrument team's expectations, and 25% better than the ETC predicts. Detector noise properties are similar to as measured on the ground, with a slightly higher 'dark current' and total noise, likely due to residuals from uncorrected cosmic ray events. The sky background is lower than predicted before flight.

Table 5 compares the ETC-predicted and actual limiting point-source sensitivity of NIRISS imaging. The limiting sensitivity is the faintest point source that can be detected at signal to noise ratio SNR=10 in an integration time of ten thousand seconds. The table quotes the pre-launch predictions from the exposure time calculator, and the predicted performance assuming the measured on-orbit throughput, PSF, and detector noise levels, and pre-flight background. This is predicted performance, not measured performance, as commissioning in general did not involve long integrations. Table 5 predicts that NIRISS parallel imaging should detect faint objects substantially faster than pre-launch expectations. The photometric stability is better than 1%, based on two measurements of the same standard star made 16 days apart.

Wavelength (μm)	1.15	2	3.5	4.4
ETC prediction (nJy)	13	10.2	14.5	22.8
Actual (nJy)	10.0	8.4	11.8	17.9

Table 5: NIRISS limiting point source sensitivity. *What is quoted is the faintest flux density that can be detected at SNR=10 in 10,000s. Values are for wide-band filters. Smaller numbers are better. The requirement level was set at 13 nJy for the 3.5 μm filter.*

The field distortion of NIRISS was calibrated using thousands of stars in the LMC astrometric field. Residual astrometric errors with respect to the catalog are 3 milli-arcsec per axis. This is better than the requirement for accurate targeting of NIRISS sources with NIRSpec multi-object spectroscopy.

The NIRISS PSF is better or similar to pre-flight WebbPSF predictions as defined by EE, FWHM and ellipticity. There is very little field-dependence of the PSF as measured by these parameters. NIRISS imaging of very bright stars shows an extra diffraction spike offset from the vertical by between -10 to +20 degrees with an angle that rotates smoothly as one moves from the right to the left edge of the detector. This spike is stronger at shorter wavelengths with an integrated intensity ~70% of the vertical diffraction spike for the shortest wavelength filter, F090W. The cause of this spike has been traced to diamond turning residual wavefront errors in some of the NIRISS off-axis mirrors.

NIRISS images show a narrow band of excess stray light running almost horizontally across the detector, dubbed “the lightsaber”. See section 6.2.5 below.

Imaging ghosts were seen in ground testing of NIRISS and similar behavior is seen in flight. They are the result of internal reflections in the optical system. Ghost positions are predictable for each filter as they form at a position that is symmetric around the ghost axis point (GAP). The GAPs for each filter were measured during commissioning and the intensity of the ghosts was found to be ~1% of the original source intensity.

The cosmic ray rate at L2 is similar to predictions. However there is a much higher rate of large ‘snowballs’ that appear as diffuse, mostly circular, events that usually saturate in their centers. See section 6.6.

6.2.2 NIRISS single object slitless spectroscopy

Time series observations of a spectrophotometric standard A-star (BD+601753, $K_{s,\ Vega}$=9.6, PID 1091, duration 5 hr) were used for flux calibration during commissioning. The median precision obtained in order 1 was 147 ppm and order 2 was 206 ppm, binned to a 22 sec integration time. This provides an independent test of the stability and precision achieved for a non-variable star, with only a low-level polynomial trend observed in spectral order 1 and no significant trends observed in orders 2 and 3. This observation was affected by a tilt event approximately in the middle of the time series resulting in a flux jump of a few 100s ppm. The tilt event was easily detected by monitoring the PSF shape along the spatial direction, more specifically by measuring the second derivative of the PSF which is a good proxy of the FWHM. The flux jump was demonstrated to be achromatic.

Observations of the exoplanet HAT-P-14 b (PID 1541, duration 6 hr) returned a point-per-point median precision in the transit depth of 85 ppm at R = 100 for order 1, and 90 ppm at R = 100 for order 2. The weighted scatter of the spectrum itself was 92 ppm for order 1 and 85 ppm for order 2. Errors in the transit depth are within <10-20% from expectations at this resolution. A tilt event was also noted early in the sequence well before ingress. The NIRISS SOSS mode readily meets performance requirements.

Throughput in this mode is 25% better for order 1 near the blaze wavelength at 1.3 µm, and ~50% better for order 2. There appears to be no significant noise penalty to operate at 70–75% of the saturation level. Observations should generally not exceed 35,000 ADUs (56,000 e-) to avoid extra noise. There is also a trade-off with observing efficiency; users may opt to saturate part of the spectrum to improve the duty cycle.

6.2.3 NIRISS wide field slitless spectroscopy

The throughput for NIRISS wide field slitless spectroscopy (WFSS, Figure 15) is generally 30% better

than expected from the ETC. As a result, the predicted on-sky sensitivities (assuming the pre-flight background model) are better than the ETC predictions by 7–20%, similar to the results in imaging mode at these wavelengths. The GR150C filter has higher throughput than GR150R at wavelengths below 1.2 μm, likely due to a different anti-reflective coating, so is preferred for F090W and F115W if only one grism is used (normally both are used to mitigate contamination).

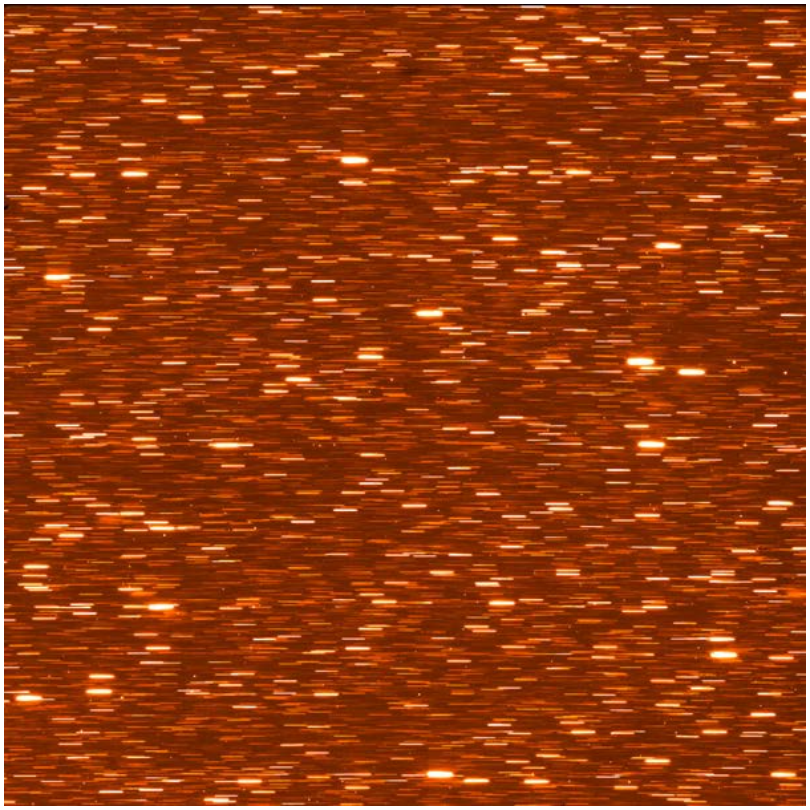

Figure 15: NIRISS WFSS. *Simultaneous spectroscopy of thousands of stars in the NIRISS focus field of the LMC. Configuration is grism GR150C and filter F115W. Data from PID 1085.*

Trace positions, curvature, dispersion and spectral resolution for WFSS are close to those measured on the ground. In addition to dispersed versions of imaging ghosts, additional ghosts due to the grisms are seen, but at a relatively low intensity level. The lightsaber scattered light feature is also apparent for WFSS. For the typical intensity where the lightsaber is dominated by zodiacal light, this emission is included in the WFSS background reference files, so will be subtracted off in the pipeline.

6.2.4 NIRISS aperture masking interferometry

The AMI mode features a seven-hole non-redundant mask that enables high-contrast (10^{-3}–10^{-4}) imaging at sub λ/D angular separations (0.1–0.5 arcsec) over three medium-band filters (F380M, F430M, F480M). This mode was successfully demonstrated through the easy detection of AB Dor C, a companion with a separation of ~0.3 arcsec with a contrast ratio of 4.5 mag (see Figure 16). The noise floor of this data set is 6.5–7.0 mag (3 sigma), very close to the photon noise floor limit of ~7.5 mag. This is the first space-based demonstration of both infrared interferometry and non-redundant aperture masking. The nominal operational concept for AMI requires staring (rather than dithering) on the science target, followed by a similar observation on an isolated reference star. Target acquisition (TA) places targets at the same detector location, and TA accuracy well within 0.1 pixel was demonstrated. In order to

investigate the effect placement errors between the science target and the calibrator, sub-pixel dithers (5-point and 25-point) were also performed.

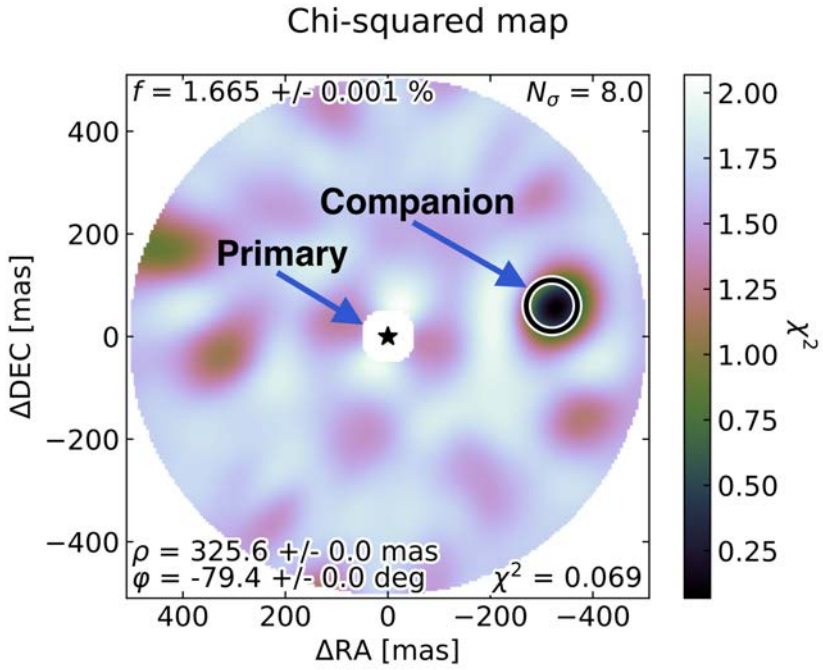

I

Figure 16: Chi-square map of AB Dor C observed with AMI at F480M. *The companion, with a flux ratio ~10^{-2} at ~0.3 arcsec, is easily detected. Data from PID 1093.*

Kernel Phase Interferometry (KPI) is the full pupil generalization of AMI used without the NRM mask but using a similar Fourier-based removal of instrument effects from the data. Like AMI, KPI also enables sub λ/D imaging but with better throughput at the price of a lower contrast at small separation. Observations were performed on 4 targets, all presumed to be single stars, but one was found to have a companion at 0.15 arcsec with a contrast of 1.7 mag. The contrast performance of both AMI and KPI are shown in Figure 17.

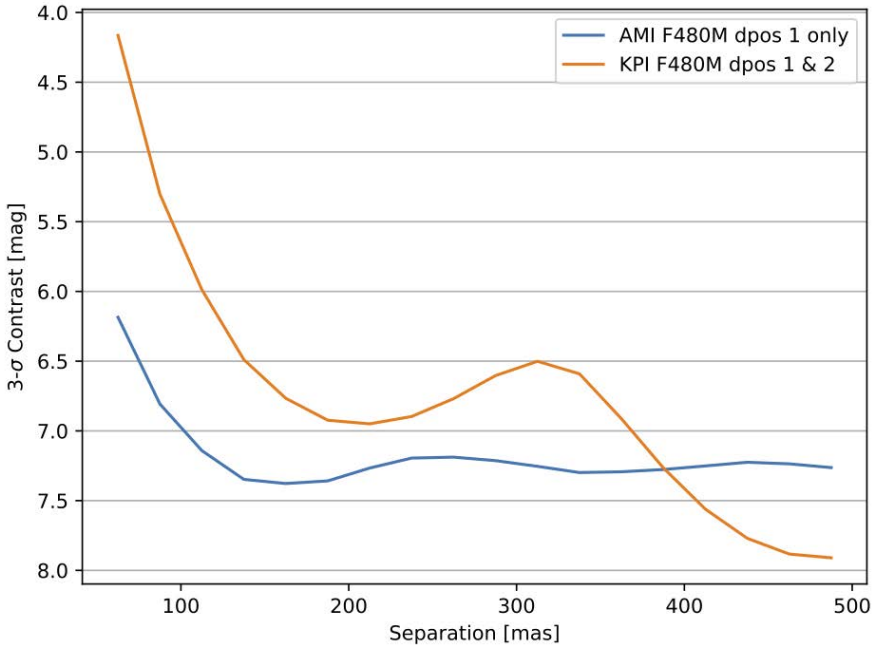

Figure 17: 3-sigma contrast performance for both AMI and KPI at 4.8 µm. *The AMI photon noise limit of this dataset is about 7.5-8 mag. The AMI and KP datasets each collected about 10^8 photons. Data from PID 1093.*

6.2.5 NIRISS stray light: the Lightsaber

NIRISS images show a narrow band of excess stray light running almost horizontally across the detector. Dubbed "the lightsaber", this light originates from the rogue path (see NIRCam claws above), grazes off the NIRISS entrance housing wall and then experiences double reflections off two mirrors inside NIRISS. See Figure 18. The light comes from a susceptibility region mapped and modeled to be far away from the NIRISS field-of-view (+2.0 deg < V2 < +5.0 deg, +12.4 deg < V3 < +12.8 deg). The zodiacal light and any stars in this region contribute to the intensity. When the light is dominated by the zodiacal light the observed brightness is typically up to 1.5% per pixel of the in-field background. When bright ($H_{Vega} \sim 0$) stars are in that region, the observed brightness is up to 10% per pixel. The lightsaber from bright stars is somewhat narrower and shifts position within the broader band caused by the zodiacal light.

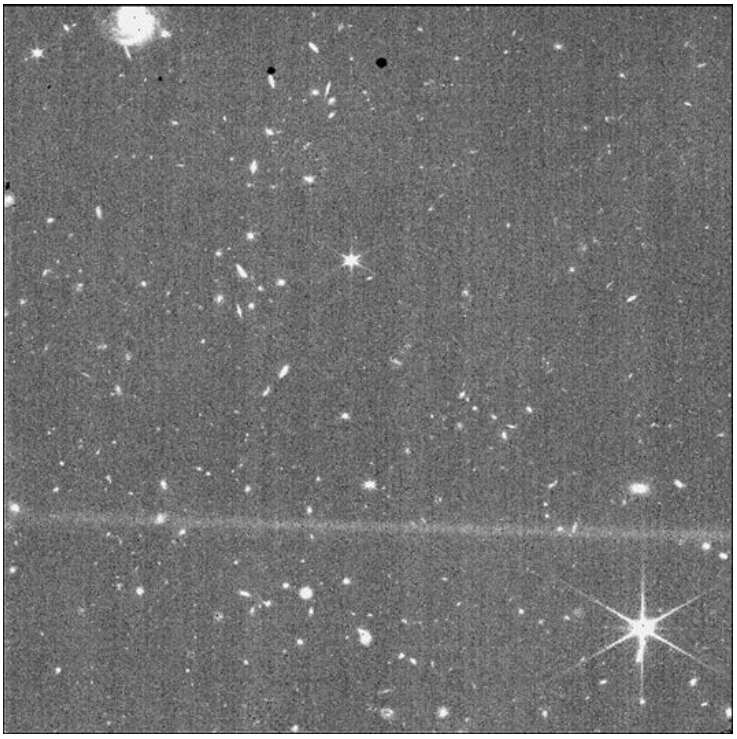

Figure 18: The NIRISS lightsaber. *This image in the F150W filter shows a prominent lightsaber stray light feature running almost horizontally across the lower part of the image. For this pointing there is a bright star in the rogue path susceptibility region. Data from PID 1063.*

Mitigation for the lightsaber comes in two forms. First, the susceptibility region has been well mapped so observations can be planned to ensure that extremely bright stars are not in that region. A tool will be developed to assist with the identification of bright targets in the susceptibility region, which will help users assess the effect of the lightsaber on a specific observation. Second, the ever-present lightsaber from the zodiacal light has been modeled and can be scaled and subtracted from images or low-resolution grism spectra. More information on this and other NIRISS features may be found at the Data Features and Image Artifacts JDox page.

6.3 NIRSpec performance

A detailed description of the NIRSpec instrument and of its pre-launch performance can be found in a series of 4 papers: overview (Jakobsen et al. 2022, A&A, 661, A80); multi-object spectroscopy (MOS) mode (Ferruit et al. 2022, A&A, 661, A81); integral field spectroscopy (IFS) mode (Böker et al. 2022, A&A, 661, A82); and exoplanet time series (Birkmann et al. 2022, A&A, 661, A83).

6.3.1 Detector noise levels

NIRSpec is equipped with 2 detectors that are used by all of its spectroscopic modes. Their performance is key to the ultimate performance of the instrument when observing faint targets because for this type of target NIRSpec operates mostly in a detector-noise limited regime. In this context, a special readout mode named IRS2 for Improved Reference Sampling and Subtraction (Rauscher et al. 2021) was developed that

achieves significantly lower noise levels.

NIRSpec commissioning was the first time the performances of the two detectors could be measured in flight and with the actual L2 cosmic-ray environment that science observations will experience. For long exposure times of 1500 s per integration, typical of faint target observations, when operating in IRS2 the two NIRSpec detectors showed noise levels similar or lower than the ETC predictions. NRS1 in particular performs 10–15% better than in the ETC predictions. Note that these measured noise levels are very complete and include not only the readout noise but also 1/f noise components, the shot noise from the dark current, as well as the residuals from the cosmic ray correction.

6.3.2 Benefits of a good telescope for NIRSpec: decreased slit losses in the MOS and FS modes

For the MOS and fixed-slit spectroscopy (FS) modes of NIRSpec, one must account for the so-called slit losses, i.e for the photons lost when masking the source by the selected slit, aperture, or micro-shutter. For a centered source, this effect is very limited (<10 %) for the largest S1600A1 aperture (1.6" x1.6") but for the 200-mas-wide slits or the micro-shutters, before the launch the losses were predicted to range between 25–50%, with the larger losses taking place at the longest wavelengths where the PSF is the broadest.

For an instrument like NIRSpec, the excellent optical quality of the telescope brings a big plus. By concentrating the light of a point source in the core of the PSF, it allows more light to go through the slit/aperture/micro-shutter. For 200-mas wide slits, the gain ranges from +2.5% at 5 μm to more than 7.5% below 3 μm, reaching more than 10% below 1 μm. This translates to a direct gain in efficiency for the instrument.

6.3.3 Efficiency of the telescope and the instrument: MOS and FS modes

As a metrics of the efficiency of the telescope and the instrument, NIRSpec uses a photon conversion efficiency (PCE), which for a given wavelength, is the ratio of the number of electrons detected to the number of photons collected. The PCE includes the telescope reflectivity, the instrument throughput, the quantum efficiency of the detectors and the slit losses. The multi-object spectroscopy (MOS) and fixed-slit spectroscopy (FS) modes of NIRSpec use very similar optical paths and, therefore, exhibit very similar PCEs for slits of similar widths (S200A1/A2/B1 and the micro-shutters).

The PCEs can be compared to the ones used by the ETC that correspond to pre-flight predictions based on measurements made at component level during the construction of NIRSpec and on the slit losses predicted before launch. See Figure 19 and Figure 20. The measured PCEs are predominantly higher than predicted, sometimes by more than 20%. The difference typically decreases toward longer wavelengths, but the relative difference is never lower than -10%.

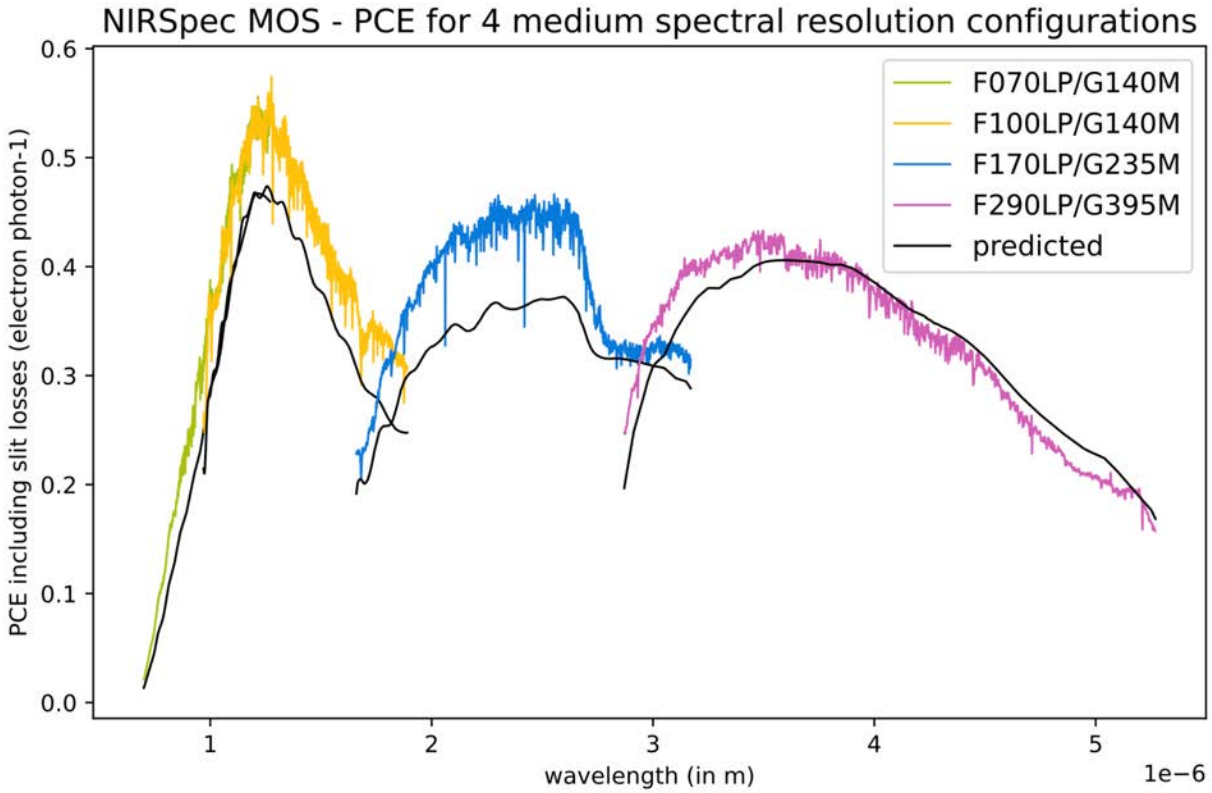

Figure 19: Measured photon conversion efficiency (PCE) for NIRSpec MOS mode and for three of the NIRSpec medium-spectral resolution configurations. *The black, solid line curves correspond to the predicted PCEs including a pre-launch model of expected slit losses. The colored curves show values measured in flight. Note that strong spikes in the measured PCEs are due to noise from bad pixels, are not real and will not appear in the final calibration reference files. In the same way, the signatures of absorption lines in the spectrum of the standard star used to measure the PCE are still present and will be removed in the final processing.*

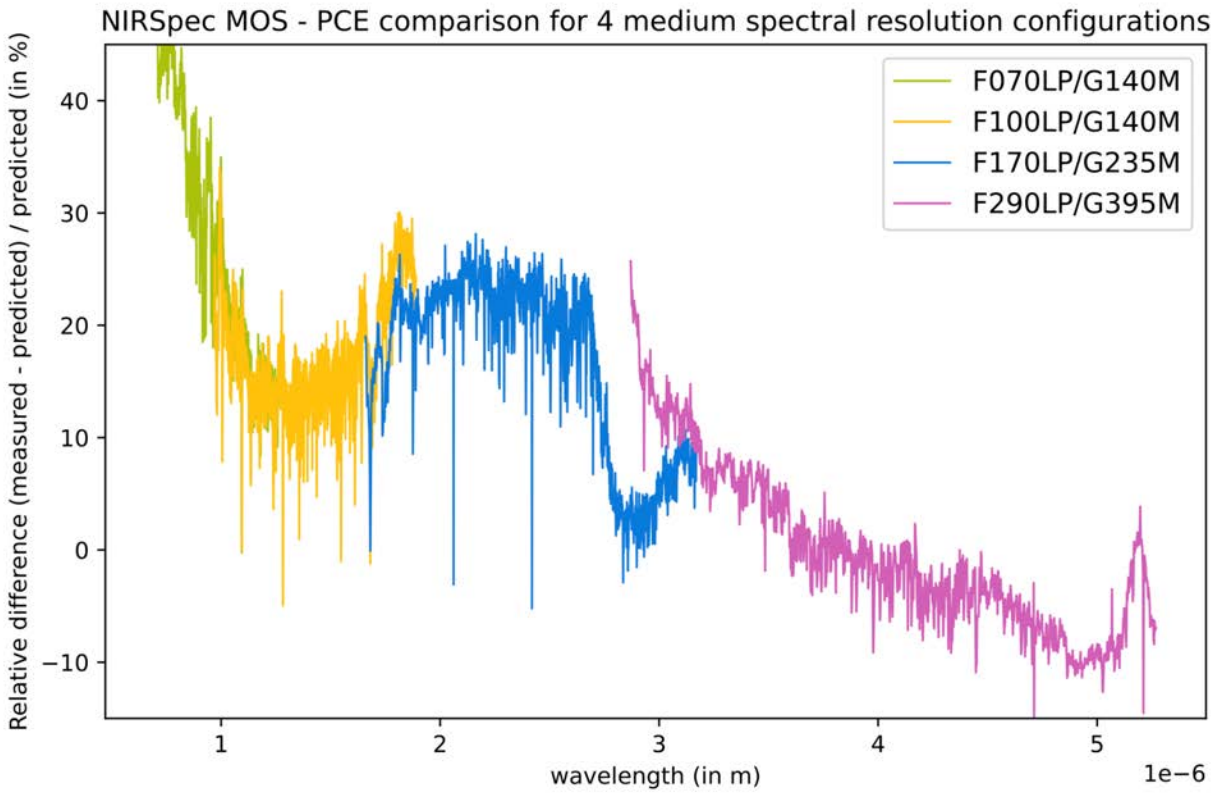

Figure 20: Plot of the difference between the measured and predicted PCEs for the same 3 medium spectral resolution configurations as in the previous figure. *This plot shows a clear trend with wavelength, with the relative difference typically decreasing toward red wavelengths but always remaining above -10%. This overall trend is observed in all spectral configurations, although bumps or drops can be present in particular for the high-spectral resolution configurations.*

Configuration MOS	**Peak PCE**	**Comparison with predictions (ETC) (measured – predicted) / predicted**
CLEAR/PRISM	~0.5 around 2 µm	From +0 to +25%
F070LP/G140M	~0.55 around 1.2–1.3 µm	From +10 to more than +40% at the blue end
F100LP/G140M	~0.55 around 1.2–1.3 µm	From +10 to +30%
F170LP/G235M	~0.45 around 2.5 µm	From 0 to +25%. Dip around 2.8–3.0 µm
F290LP/G395M	~0.40 around 3.5 µm	From -10 to +20%. Lower than predicted > 3.5 µm
F070LP/G140H	~0.55 around 1.2–1.3 µm	From +15 to > +40% toward the blue end
F100LP/G140H	~0.55 around 1.2–1.3 µm	From +10 to +30%

F170LP/G235H	~0.45 around 2.3 µm	From 0 to > +40%. Dip around 2.8–3.0 µm.
F290LP/G395H	~0.45 around 3.6 µm	From -10 to > +30%. Lower than predicted > 4 µm

Table 6: Summary of photon conversion efficiency for NIRSpec MOS mode. *For the nine spectral configurations, the table quotes the peak PCE and quotes the relative differences with the predictions used in the ETC. Very similar results are obtained for the FS mode.*

6.3.4 Efficiency of the telescope and the instrument: IFS mode

The integral-field spectroscopy (IFS) mode of NIRSpec has a more complex optical path than the MOS and FS ones. It includes an additional integral-field unit (IFU) containing a series of mirrors used to cut the image of an object into 30 slices and to project them back into NIRSpec spectrograph in two groups of 15 slice images that can be dispersed without overlapping. Therefore, the PCE of the IFS mode includes an additional component, the efficiency of the IFU module.

In addition to that, the slicing of the image of the object with small (100 mas wide) slices will generate additional diffraction in NIRSpec spectrograph, creating additional losses. For point sources, these diffraction losses are predicted to reach slightly more than 10% at the longest wavelengths. These losses cannot be disentangled from the PCE measurements and will therefore be included in the measured PCE for the IFS mode. These were not included in the PCE values provided to the ETC, making them too optimistic, in particular in the red.

The measured PCEs for the IFS mode (Figure 21) show similar trends than for the MOS and FS mode but with more pronounced deviations from the expected values. This is clearly illustrated when comparing the measured and predicted PCEs for the CLEAR/PRISM configuration, which cover the full wavelength range of NIRSpec. In the blue, the PCE is typically better than predicted with excesses well above 20% at some wavelengths. In the red, the measured PCE curve moves below the predicted one, decreasing with wavelength and with relative differences up to -20% instead of the -10% observed in the MOS and FS modes. The difference with the other modes can probably be explained by the fact that the diffraction losses were not included in the predicted PCEs delivered to the ETC.

6.3.5 NIRSpec fixed slit spectroscopy (FS) Performance Summary

The NIRSpec fixed-slit spectroscopy (FS) mode is operating nominally and the associated target acquisition (Wide-Aperture Target Acquisition = WATA) is working (see section 3.2), allowing to position the scientific target in the slits/apertures with an accuracy better than 20 mas.

The in-flight sensitivity of the FS mode is the result of the combination of the measured detector noise levels and of the measured efficiency of the telescope and the instrument. When observing faint objects, NIRSpec is detector-noise limited and both contributors have a linear impact on the resulting signal to noise ratio. The in-flight detector noise levels are either similar to or better than predicted (see section 6.3.1) while the in-flight efficiency is typically higher than predicted but with some wavelengths that can be up to 10% lower than predicted (see sections 6.3.2 and 6.3.3). If we combine the two, this indicates that the FS mode is expected to achieve sensitivity levels either better or very similar to the predicted ones.

6.3.6 NIRSpec integral field spectroscopy (IFS) Performance Summary

The NIRSpec integral-field spectroscopy (IFS) mode is operating nominally. Although the associated target acquisition (Wide-Aperture Target Acquisition = WATA) is working (see section 3.2), a problem with the astrometric solution for this specific mode has temporarily introduced a bulk offset of approximately 200 mas. A fix is in progress and as soon as it is in place, we expect to be able to position the scientific target in the IFS field of view with an accuracy better than 20 mas.

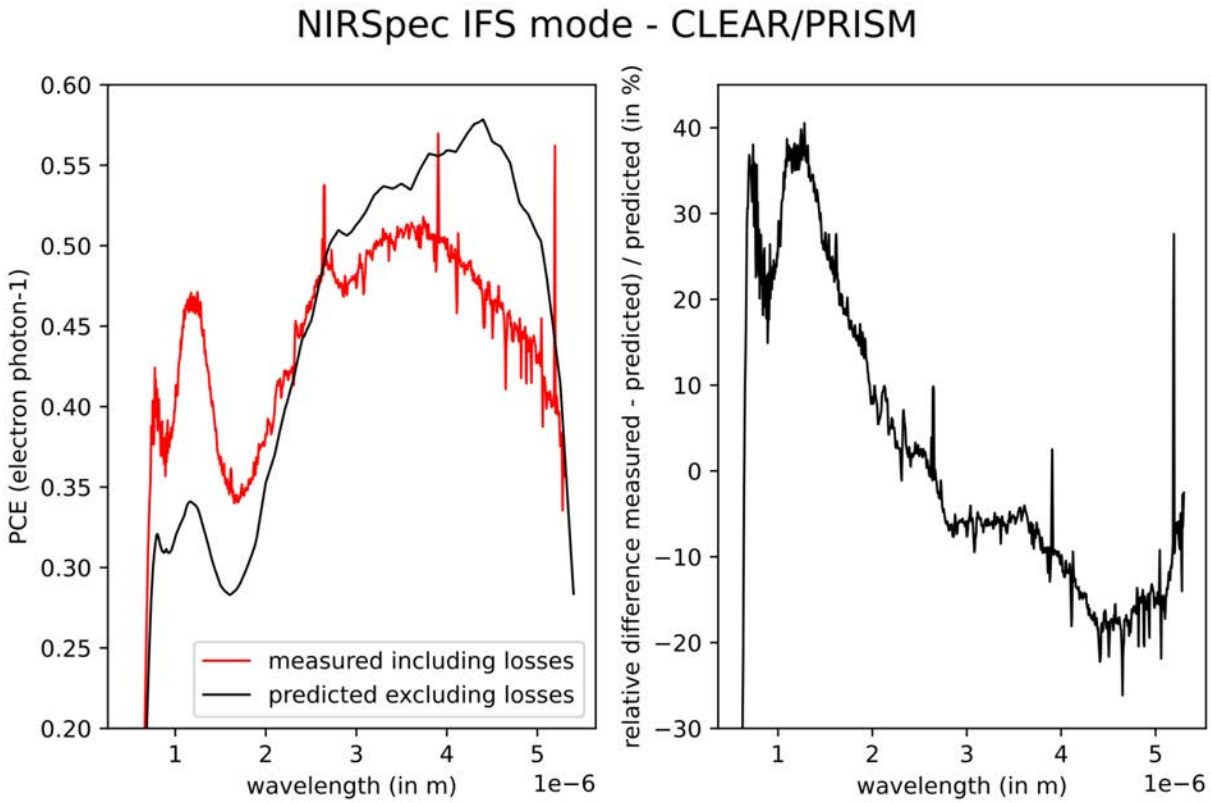

Figure 21: The measured photon conversion efficiency for the CLEAR/PRISM configuration of the NIRSpec IFS mode. *The black, solid line curves correspond to the predicted PCE. Note that strong spikes in the measured PCEs are due to bad pixels, are not real and will not appear in the final calibration reference files.*

As for the FS mode, the sensitivity of the IFS mode is the combination of the measured detector noise levels and of the measured efficiency of the telescope and the instrument. In the case of the IFS, the detector noise levels are identical to those for the FS mode while the measured PCEs have stronger departures (in both directions) compared to the predicted ones. Therefore, for the IFS mode we expect some degradation of the sensitivity compared to the predicted one in the red (-10 to -20%), accompanied by a significantly better than predicted sensitivity in the blue (> 20% improvement).

6.3.7 NIRSpec multi-object spectroscopy

The NIRSpec multi-object spectroscopy (MOS) mode is operating nominally. See Figure 22. The associated target acquisition (Microshutter Assembly Target Acquisition = MSATA) is working (see section 3.2).

Experience gained during the commissioning with the MSATA has confirmed the need to have an excellent relative astrometry between the scientific target and the reference stars (5–10 mas). It has also highlighted the need for good absolute astrometry for the reference stars with respect to the Gaia celestial reference frame, both in terms of residual offsets (better than a few tenths of an arcsecond) and rotation (better than 0.03 degrees). The NIRSpec MOS mode documentation is being updated to reflect these requirements and particular attention must be paid to these aspects when the final MOS observations are submitted by the observers.

Like for the other modes, the in-flight sensitivity of the MOS mode is the results of the combination of the measured detector noise levels and of the measured efficiency of the telescope and the instrument. When observing faint objects, NIRSpec is detector-noise limited and both contributors have a linear impact on the resulting signal to noise ratio. The in-flight detector noise levels are either similar or better than predicted (see section 6.3.1) while the in-flight efficiency is typically higher than predicted but with some regions that can be up to 10% lower than predicted (see sections 6.3.2 and 6.3.3). If we combine the two, this indicates that the MOS mode is expected to achieve sensitivity levels either better or very similar to the predicted ones.

The ultimate performance of the MOS mode is also linked to the multiplex levels that can be achieved, to the number of objects that can be observed simultaneously using the baseline MOS-mode observation strategy, i.e. when using a 3-point nodding with the objects placed in slitlets made of 3 consecutive micro-shutters. Within the NIRSpec MOS field of view (limited by a field stop at the entrance of NIRSpec), the operability rate of the micro-shutters is currently 82.5%. Of the 17.5% of these micro-shutters that are not operable, 7% cannot be opened at all while 10.5% cannot be operated because they belong to rows or columns that have been masked due to the presence of electrical shorts. Additional shorts have been detected and masked during the commissioning and close monitoring is being put in place during operation.

In addition to these failed-closed shutters, a very small number of shutters cannot be closed and are classified as failed open. Their number has remained stable with only two new failed-open shutter detected within the MOS field of view during commissioning, for an updated total of 22.

The multiplexing levels have remained within 10% of the pre-launch levels and are still excellent with, for high target densities, the possibility to observe more than 200 scientific targets at a time at low spectral resolution or close to 60 at medium / high spectral resolution.

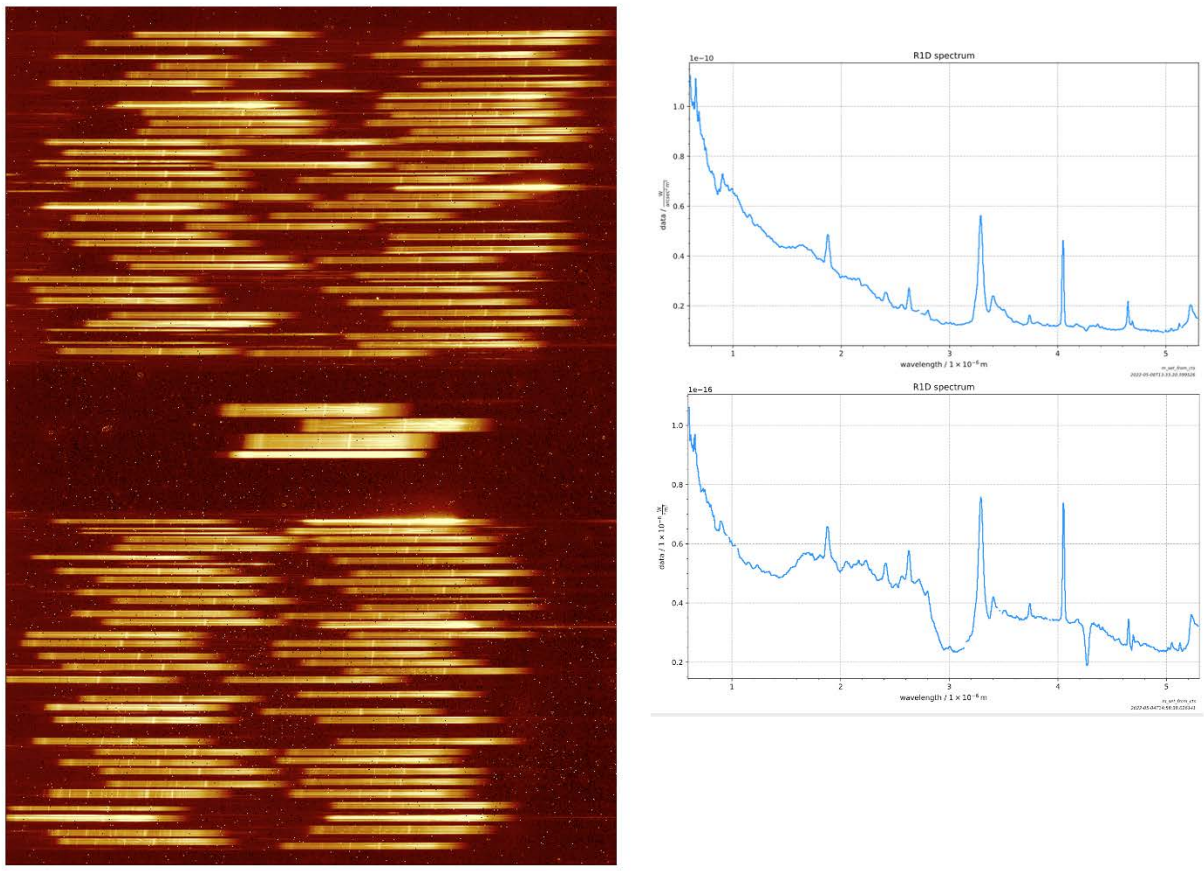

Figure 22: Multi-object spectroscopy with the NIRSpec microshutter array. *The low-spectral resolution prism mode was used, with a total of 235 1x3 microshutter slitlets opened, to capture spectral features from the diffuse interstellar medium in a region close to the Galactic Center. Extracted, uncalibrated example spectra show multiple emission and absorption line features. Data from PID 1448.*

6.3.8 NIRSpec bright object time series

NIRSpec bright object time series observations require the use of Wide Aperture Target Acquisition (WATA), which was successfully demonstrated for fixed targets during commissioning, including for HAT-P-14 b. NIRSpec observations of HAT-P-14 b (PID 1118) spanned 6 hours and used the square 1.6” x 1.6” aperture and the G395H grating. Results were nominal: At R=100, the precision in the transit depth in the NRS1 detector was 50 ppm per point; in the NRS2 detector it was 66 ppm per point. Errors in the transit depth were < 10% from expectations. No persistence ramp was seen. The traces were extremely stable, moving by about 0.0002” RMS, with no significant drift with time. Some wavelengths will saturate faster than expected, due to better than predicted PCE at some wavelengths.

6.4 MIRI performance

6.4.1 MIRI imaging

The MIRI imager sensitivity exceeds the ETC predictions by typically 10% across the wavelength range. Overall MIRI imaging is working as expected. The PSFs (see Figure 23) closely match WebbPSF predictions, with the exception of known differences with the cruciform artifact at short wavelengths.

Measured FWHM and encircled energies are within a few percent of expectations for all filters and field positions.

Latent image characteristics are very good. Latents from very bright sources have been shown to dissipate to < 0.01 % of the imprinting source signal within 15–30 minutes. Cooler-assisted annealing of the detector has been verified to work well to remove latent images.

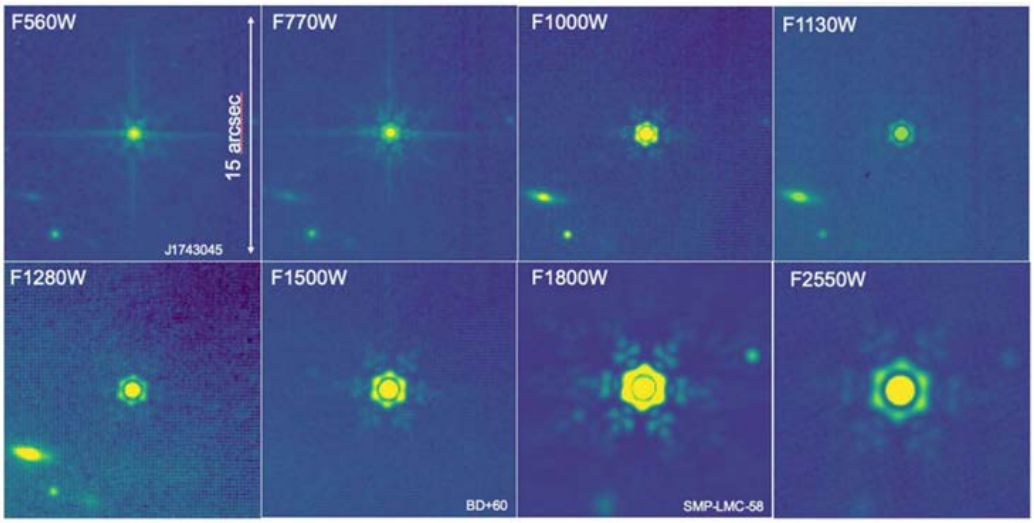

Figure 23: Examples of the MIRI imager PSF in eight of the nine available filters.

Calibration data products including darks and flats have been produced for the imager which have been shown to improve the imaging products at all wavelengths. Further improvements to calibration data products will be made. Sky flats do not remove background structure well at the longest wavelengths. The large backgrounds may leave residuals unless observers take dithered exposures toward adjacent fields to remove the background by differencing or use a median filter technique.

Some scattered light originating in the observatory (with an apparent temperature ~120 K) is observed in the imager along the edges of the structure that separates the imager field from the coronagraphic fields; it is confined to a small number of rows and columns near the edge of this structure, particularly near the "diving board", and along the rows at the bottom of the detector (lowest row numbers, see Figure 24). Because this light enters off the telecentric angles, it is removed by the internal stops, e.g., the pupil stop, and is only seen where structures in the physical focal plane of the instrument scatter it into the range of angles that pass the internal stray light rejection. The stray light observed at the edges of structures in the imager focal plane is not regarded as having any significant impact on imaging science performance.

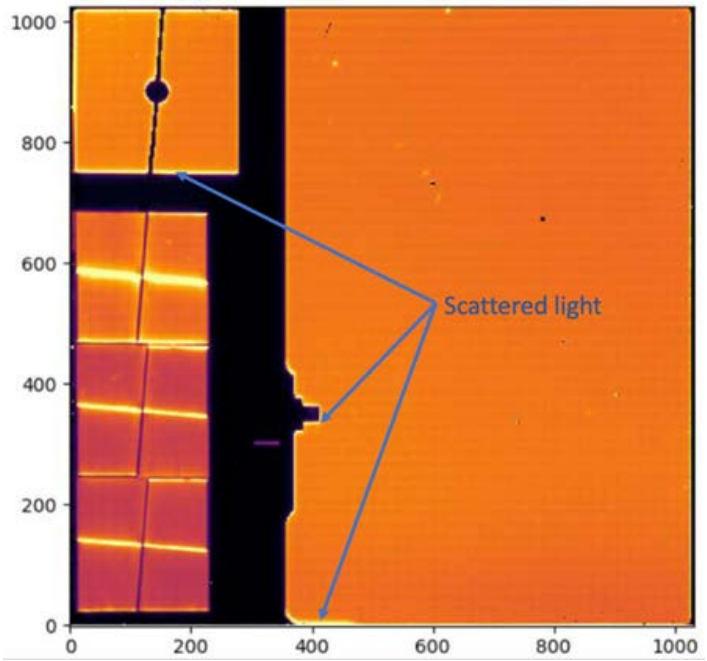

Figure 24: Imager focal plane showing areas of scattered light around the edges.

MIRI imaging photometric stability was investigated in commissioning with observations of two spectrophotometric standards BD+60 1753 and J1743045 (PID 1027), which were observed twice with a separation of over a week. All photometric measurements (at 80% encircled energy) agreed to within 5%. Good photometric stability was also demonstrated in the transit test observation discussed below.

Finally, MIRI imaging dither patterns were tested and function nominally, and are deemed essential for good performance. There is early evidence that dithers with larger steps give better results in terms of mitigating latents, bad pixels, and deriving backgrounds from the data set.

6.4.2 MIRI low resolution spectroscopy

The MIRI Low Resolution Spectroscopy mode performs as expected, with excellent image quality that matches the WebbPSF predictions to within 5%. Some small variations are observed between slit and slitless operation which is in line with expectations. The relative calibrated spectral response for LRS matches the spectrophotometric standard to better than 5% over the full 5–12 μm bandpass. The measured in-orbit sensitivity of the LRS slightly exceeds the ETC estimates, though in general the ETC performs adequately for LRS with regards to sensitivity and saturation. The observed discrepancies in the observed and predicted counts are being investigated.

The latest flight calibration files extend the wavelength and flux calibration of the spectra to a wider range, from approximately 4 to 14 μm; these will be available shortly after the data release. The accuracy of target placement with target acquisition (TA) is around 10-15 mas along the detector y-axis, which is sufficient for achieving good calibration. For observations that include TA using the science target itself (not offset TA), users are strongly recommended to request a TA verification image. These images are extremely useful in checking the placement accuracy. For slitless observations, verification images are already obtained by default. Users are also advised to check the accuracy of the automated extraction, and perform a manual extraction in case of any suspected inaccuracies.

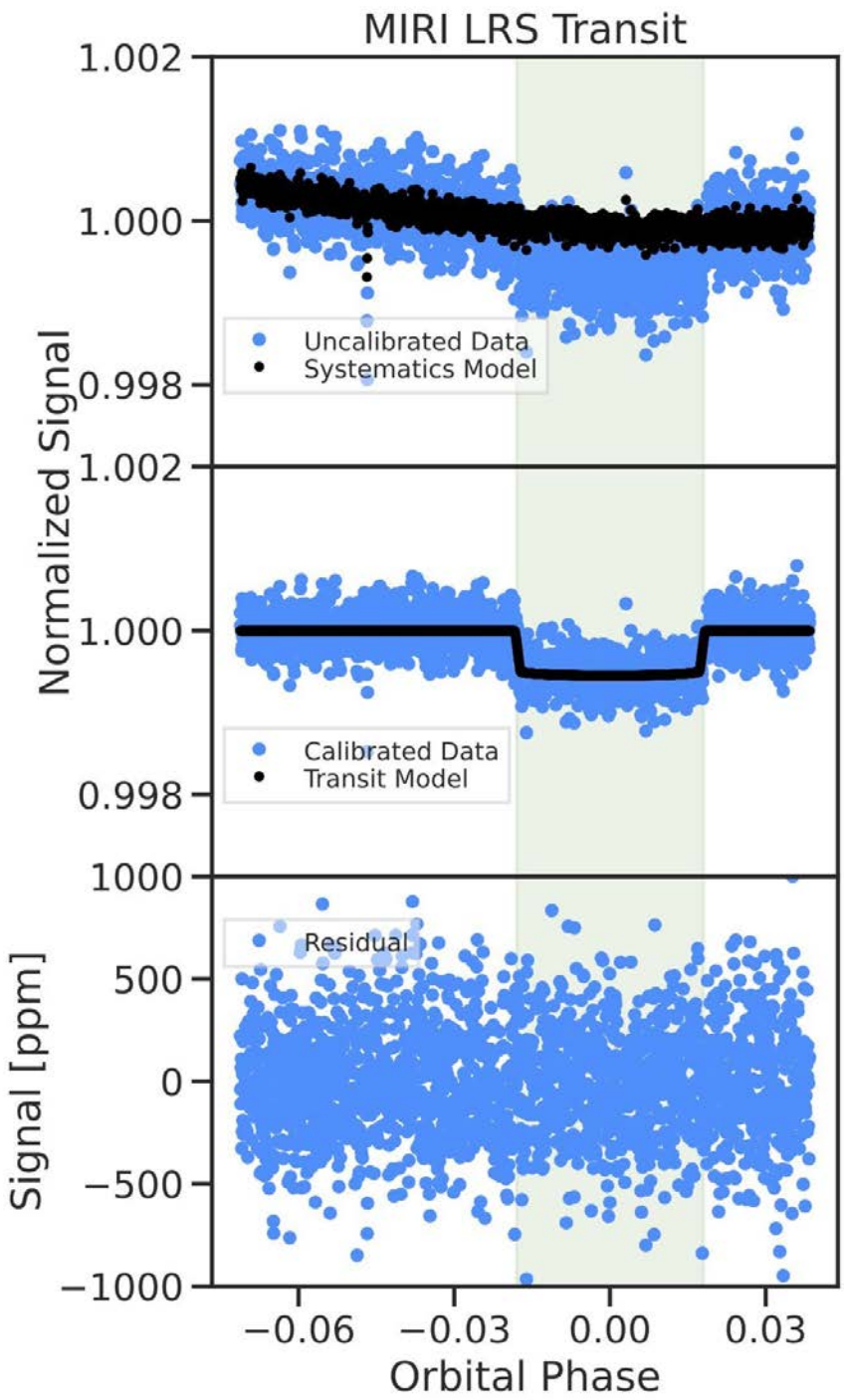

Figure 25: Transit observation of the exoplanet L168-9b, as measured with the MIRI LRS in slitless mode. *Data were obtained from a single primary transit measurement, covering a total of 4.2 hours. The top panel shows the white-light curve together with a model estimate of the systematics. The middle panel shows the systematic-free white light curve and the fitted transit model. The bottom panel shows the residual after subtracting the transit model. Note that each point is an average of 4 integrations (~6 seconds). Data from PID 1033.*

Scattered light may contaminate the science spectrum if a very bright target is found close to the science target, even if it is located behind the focal plane masking structure or in the imager field of view. For slitless LRS the automated pipeline does not yet perform any subtraction of the background. We recommend computing a background from the off-target subarray regions for each integration individually, and subtracting this per integration (rather than producing a single co-added background); this provides the best correction for the background and other noise sources.

The MIRI LRS time series observation (TSO) test involved observing a primary transit of the L168-9b planet (aka TOI-134; PID 1033, Observation 5). This is a super-Earth orbiting a K=7.1 (Vega) magnitude star with a period of 1.4 days and a transit time of 1.19 hrs. The full exposure duration was 4.2 hrs, covering a single transit, and ample detector settling and out-of-transit time. The transit was easily recovered in the MIRI data, and the spectro-photometric precision following our current best calibration was ~50 ppm at a spectral resolution of R~50 at 7.5 μm (this corresponds to averaging about 6 detector pixel rows). Initial detector settling time was approximately 20 mins, during which a drift of ~0.3% was seen in the (band averaged) detector response. A slow drift with a magnitude of about 500 ppm could be observed during the rest of the spectral time series. Over the duration of the exposure, the pointing stability was extremely high (<< 0.1 pixel in both axes and limited by measurement precision). Movement was detected in only a handful of integrations; this was linked to a high gain antenna movement, as permitted with continuous time series observations, and had no impact on the final performance.

6.4.3 MIRI medium resolution spectroscopy

The absolute throughput for MIRI MRS has been measured using the photometric standard single star HD163466 for all MRS bands. The sensitivity was tested using both the spatial SNR, measured with aperture photometry on the 3D-cube, and the spectral SNR, measured from an extracted spectrum. The spatial SNR meets or exceeds pre-launch expectations in all 12 MRS bands. The spectral SNR meets pre-launch expectations for all but Channel 3 and channel 4A, where it apparently dips to ~40% below predictions, likely due to residual spectral fringes in the data.

Since the absolute flux calibration is presently based on observations of a single star, there are some artifacts in the present calibration longward of ~20 μm that will be improved throughout Cycle 1 as more calibration data are obtained. Observations of the star HD 159222 separated by 1 week showed photometric response that was repeatable to better than 10%. No other time series tests using this mode were performed during commissioning. The wavelength calibration of the MIRI MRS data is generally accurate to within ~1 spectral resolution element (~100 km/s). Astrometric calibration is currently accurate to ~0.25 pixels, with some residual slice offsets and plate scale mismatches to be corrected during Cycle 1.

The scattered light is an integral part of the MRS PSF, which is a telescope diffraction-limited PSF, convolved by the MRS detector response function to incoming illumination. The origin of the measured scattered light in the MRS is caused by the known photon scattering inside of the MRS detector substrate. This photon scattering in the MRS detectors manifests in the data in two ways: 1) A broader PSF FWHM compared to diffraction limited PSF predictions, and 2) secondary diffraction at narrow gaps between the pixels, which act as narrow slits in the mid-infrared. This superimposes a traditional Airy diffraction pattern on the detector that is centered on the PSF. Because neighboring slices on the detector do not correlate to neighboring pixels on the sky, the wings of the Airy diffraction pattern will appear in the MRS 3D-reconstructed spectral cubes as faint emission away from the observed point source. Additionally, neighboring slices on the detector are offset in wavelength. This means that the wings of the diffraction

pattern produced at one wavelength will result in a faint emission line at a different wavelength (and location on the sky) see Figure 26. A correction for the spatial scattered light has been implemented in the current pipeline and reduces residuals from 20% of the total flux to 1%.

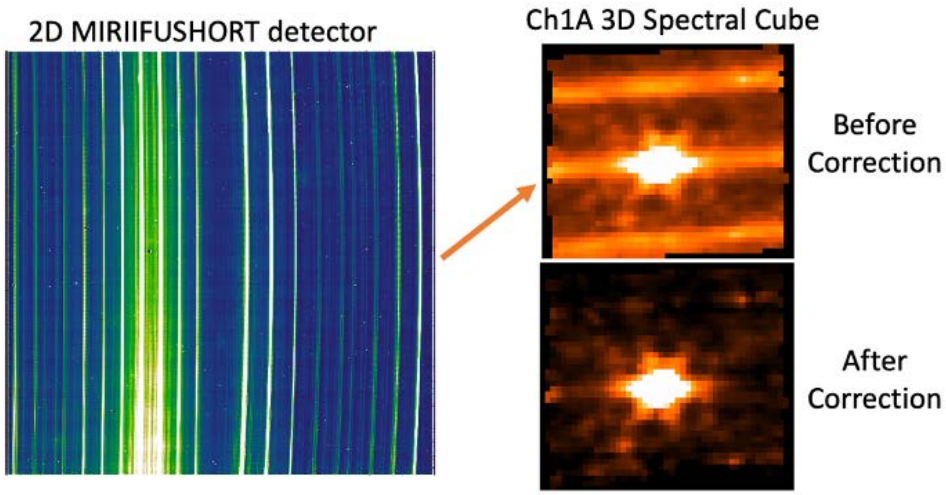

Figure 26: Left: 2-D detector view of MRS scattered light. Right: In 3-D cubes the scattered light manifests as horizontal bars across the spatial cube. *After correction, the scattered light in the cube is reduced from 20% of the total flux to 1%.*

MRS data contain fringes: large-amplitude sensitivity modulations with wavelength, caused by standing waves in the detector and in the dichroics. Fringes change across the MRS wavelength range. Amplitudes are highest at low wavelengths (up to ~40% peak to peak). From channel 2C onward, fringe amplitude varies across the band due to beating. On the MIRIFULONG detector, we see an additional low-amplitude high-frequency modulation that is tentatively attributed to fringing within the dichroics. Two pipeline steps plus a post-pipeline notebook are available to correct for fringes. Taken together, they reduce fringe contrast to safely below 6%.

MRS commissioning data were all taken using the FASTR1 detector mode. The SLOWR1 mode reference files are in progress and the pipeline will be updated for this mode in the near future.

6.4.4 MIRI coronagraphic imaging

The MIRI coronagraphs' performance exceeds expectations. JWST commissioning successfully demonstrated target acquisition (TA) in quadrant one (1) of each four-quadrant phase mask (4QPM) to a precision of 10 mas. The TA for the Lyot is accurate and precise to ~20 mas for quadrant one (1) TA. Coronagraphic TA has not yet been demonstrated using quadrants 2, 3 & 4. Target acquisition may be performed in one of four user-selectable filters: F560W, F1000W, F1500W, and a neutral density filter (FND). During commissioning, only the FND was fully verified for TA; the other TA filters will be verified for TA during Cycle 1 calibration programs. Latent images from the TA process do not appear to be a significant problem for MIRI, especially for sources that avoid saturation, so users who have chosen to avoid Quadrant 1 for this reason may reconsider this choice in order to improve the schedulability of their observations. Note that the MIRI team is still evaluating the impact of latent images, so we recommend consultation with the MIRI team before making any changes.

Flight data have shown that there is scattered light at the edges of the coronagraphs' image plane optics. The source of scattered light does not appear to be celestial; it is likely thermal emission from the telescope/observatory and does not vary significantly with pointing. This is particularly apparent for the three 4QPMs, where it manifests as a glow along the horizontal boundaries of the phase masks (Figure 27). The features are referred to as "glow sticks." Scattered light is also seen in the Lyot coronagraph (Figure 28), particularly around the top half of the Lyot spot and the bottom of the FOV.

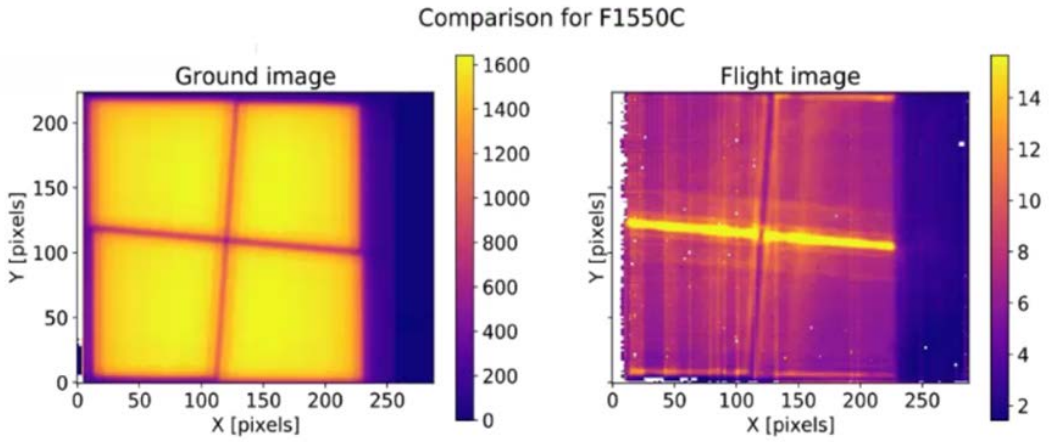

Figure 27. Comparison between the ground and flight images of the F1550C coronagraph when uniformly illuminated. *The Glow Sticks feature is clearly visible, and "hides" the attenuation of the 4QPM phase mask along the horizontal axis. This feature is seen in all three 4QPMs.*

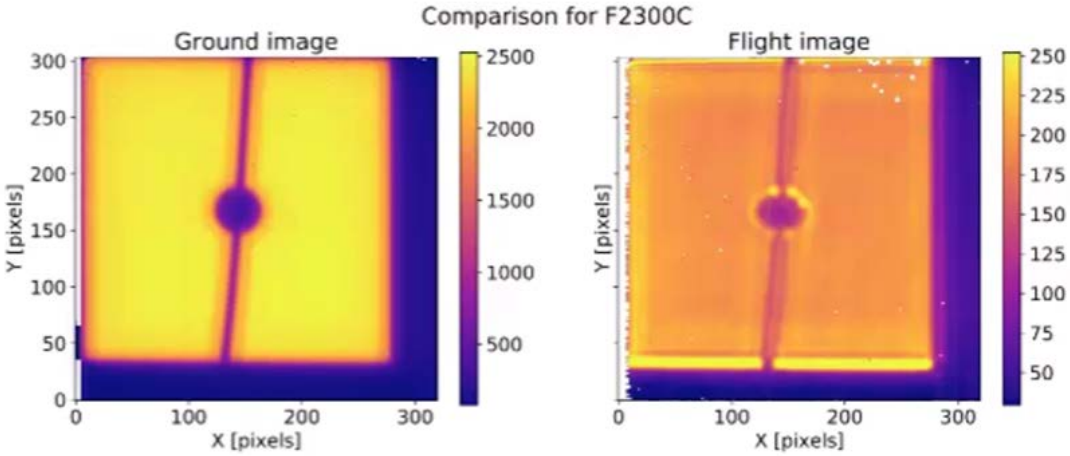

Figure* 28: *Comparison between the ground and flight images for the Lyot coronagraph when uniformly illuminated. *The scattered light is evident along the upper edge of the Lyot spot, and the lower edge of the coronagraph FOV.*

These scattered light components can be removed by obtaining dedicated background observations. It is very important that the background observations be obtained with the exact exposure parameters used for the main target (the same as for one of the dithers, if using the Small Grid Dither pattern). This also means a background observation should be obtained separately for science targets and reference star PSF

observations. After subtraction, these scattered light features appear to mostly increase the shot noise in the region of the boundaries/edges. More information on this and other MIRI features may be found at the Data Features and Image Artifacts JDox page.

To achieve science mode readiness, the MIRI 4QPM coronagraphs needed to demonstrate a raw contrast better than 2400 (pre-PSF subtraction), and the Lyot coronagraph needed to demonstrate a raw contrast better than 1200, all at 6λ/D (Note, MIRI coronagraph contrasts listed here use the reciprocal definition compared to the NIRCam coronagraph section). The contrast seen in the 1140C 4QPM is better than requirement–level expectations at all separations where photon noise does not dominate. Table 7 summarizes the raw contrast of all MIRI coronagraphs.

Coronagraph	MASK1065	MASK1140	MASK1550	MASKLYOT
Raw contrast (6λ/D)	10,570 ± 240	12,700 ± 330	14,700 ± 480	10,260
Rejection (3λ/D)	108.1 ± 8.8	108.8 ± 5.6	135.8 ± 7.1	233.5
Star subtraction (3σ at 6λ/D)	61,800	47,300	24,100	N/A

Table 7: Measured contrast and rejection ratios for all MIRI coronagraphs.

Commissioning directly tested the impact of slew size on PSF-subtracted contrast for MIRI coronagraphy, by using PSF reference stars located ~1 deg and ~10 deg from the target star. No significant difference in the final PSF-subtracted contrast was observed for reference PSFs obtained sequentially with the science target. The "shelf-life" of reference PSFs, and the parameters governing it, are under investigation.

6.5 Using two science instruments in parallel

JWST supports parallel observing, in which two science instruments are used simultaneously. There are two types of parallel: coordinated parallels and pure parallels.

6.5.1 Coordinated parallels

Coordinated parallels are when two science instruments are used together for the same observing program. A total of 170 coordinated parallel visits were successfully executed during science instrument commissioning (Figure 29), and worked well with only one issue (discussed just below). Parallel operations are designed such that mechanism movements of each instrument do not disturb the operation of the other; this coordination is working as designed.

While there was no requirement that all of the eleven coordinated templates be exercised during commissioning, in the end seven of the templates were. The four templates that were **not** exercised are: NIRCam Imaging + NIRISS WFSS; NIRCam WFSS + MIRI Imaging; NIRCam WFSS + NIRISS Imaging; and MIRI Imaging + NIRISS WFSS. We see no reason why these templates should not work, as these WFSS templates are identical to the imaging templates except for putting a grism in the beam instead of a filter.

The one issue with parallel observing that was identified was this: when all 10 NIRCam detectors were used in parallel with another instrument, data from one instrument could under some circumstances be

partially overwritten by data from the other instrument. Flight software was patched on 24 June 2022 to fix this issue. Data taken earlier may be affected by partial data overwrite.

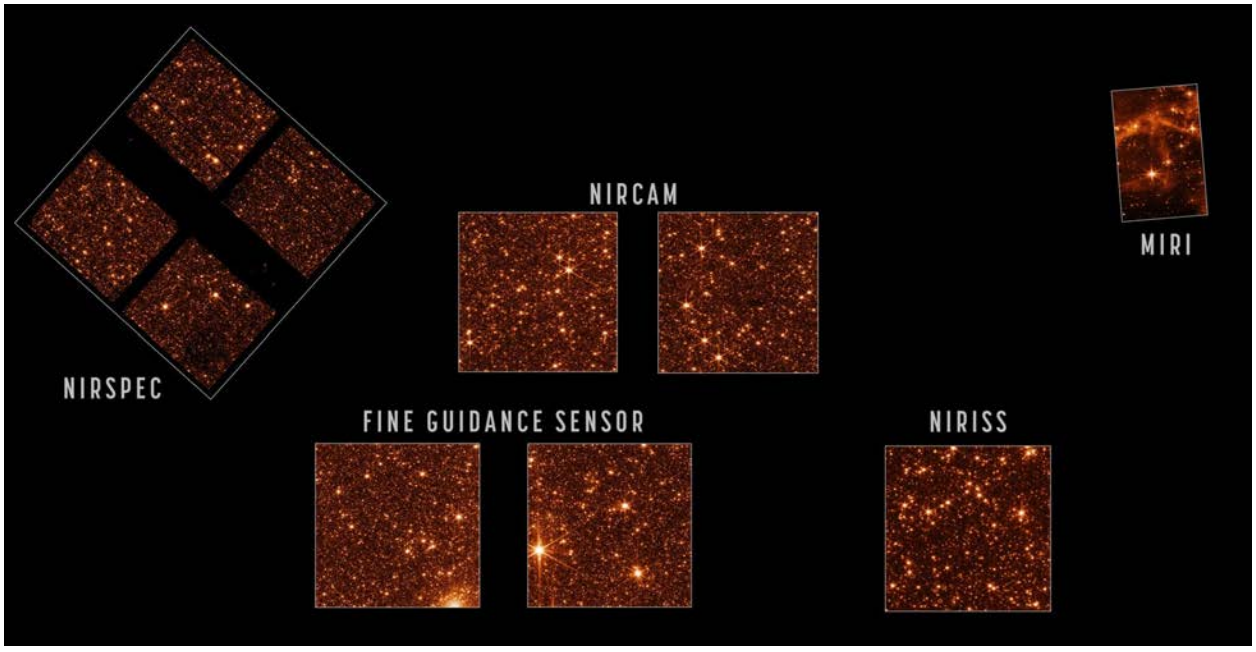

Figure 29: Observations of the JWST astrometric calibration field and surroundings in the Large Magellanic Cloud. *These observations from PID 1473, previously released, were taken just after the completion of multi-instrument optical alignment to assess and demonstrate image quality in all instruments. This also served as an engineering test of coordinated parallel operations: this included the first uses of NIRCam+MIRI imaging, MIRI+NIRCam imaging, and NIRSpec MOS spectroscopy+NIRCam imaging, as well as NIRCam+NIRISS imaging and NIRCam+FGS imaging, with many combinations of filters and parallel-optimized dither patterns. The pointings on sky are all shown in the correct relative orientations and scales relative to one another.*

6.5.2 Pure parallels

Pure parallels are when an observing program makes use of parallel observing opportunities from other accepted proposals. Thus, in pure parallel mode two science programs execute at once. Pure parallel mode was not exercised in commissioning. Pure parallel programs will not be scheduled for the first three months of Cycle 1. The reason is the tight (11%) margin on data downlink in Cycle 1. Data volume is used as a constraint when scheduling JWST observations; the schedule is built to keep the onboard solid state recorder from filling, since if the recorder fills JWST would halt observing and sit idle until the next ground contact. The project will assess how well data volume is managed through scheduling and downlink performance in the first few months of Cycle 1, to determine if and when pure parallel observing can begin.

6.6 Cross-instrument detector topic: cosmic rays

Observed cosmic ray rates and properties are largely in line with expectations. The vast majority of cosmic ray impacts directly affect only one or 2 pixels, but there are also uncommon events that affect hundreds of pixels. These are thought to arise from relatively low energy secondary atomic particles that deposit all of their kinetic energy into the detector. These large events are colloquially termed snowballs.

There are also large radiation events that affect the MIRI detectors; because these do not have a generally circular morphology they tend to not be termed snowballs but are called "shower" events.

The current JWST data reduction pipeline handles the first order effects from cosmic ray events but the large number of electrons that result from a snowball event have secondary effects that are not currently corrected in the pipeline. Residuals have a circular appearance with alternating light and dark bands a few tens of pixels across. Dithering exposures is the current recommended mitigation strategy. A four-point or larger dither pattern will allow the pipeline outlier detection routine to significantly improve the final combined image. Work is in progress to improve the calibration pipeline's detection and handling of regions affected by snowballs.

7.0 Science Operations Status

Science operations includes managing the proposal process, preparing visits for execution, processing data from the observatory, and making data products available via the MAST archive. JWST science operations at STScI provided outstanding service during commissioning and the transition to Cycle 1. Complex software and processes worked thanks to many tests and rehearsals prior to launch. Planned updates and unexpected issues were handled via operational work-arounds and software updates. Nevertheless, some significant issues remain and warrant attention, as discussed below.

The onboard scripting subsystem (OSS) carries out the science observations by executing the Observation Plan (OP), which is uploaded weekly and executed by OSS autonomously, often while JWST is not in contact with the Mission Operations Center. OSS was used to conduct most of the telescope and science instrument commissioning activities, and has been patched several times to resolve issues identified during commissioning.

The JWST Exposure Time Calculator (ETC) reflects pre-launch expectations. As described above, end-to-end flight performance is typically better, in some cases by a significant amount. The ETC will be updated shortly before release of the Cycle 2 Call for Proposals in November, after detailed analysis of flight data. In the interim, observers may use performance information above and in JDox to scale ETC results. For the typical case of higher than expected throughput, the main concern is unexpected saturation during target acquisition or early in an integration. Saturation later in an integration will generally yield S/N comparable to or better than predicted by the ETC.

The Astronomer's Proposal Tool (APT) and the MSA Planning Tool now reflect flight measurements of aperture placement in the focal plane and distortion across instrument apertures. Additional refinements are expected, but the impact on observers should be negligible. Functionality will also evolve slightly to accommodate insights from commissioning.

Long range plan windows have been published for most Cycle 1 visits. Investigators can search for program information and click the Visit Status Information link for more information. Whenever possible, visits are scheduled and executed within their assigned plan window, but operational issues may cause plan windows to change, visits not to schedule, or scheduled visits not to execute. This is particularly true early in Cycle 1. Visits that do not execute are usually rescheduled.

JWST uses the Guide Star Catalog (GSC) to specify astrometry and photometry of guide stars and reference stars for guide star acquisition. During commissioning, a few guide star acquisitions failed because the guide "star" was actually a galaxy resolved by FGS or because coordinates in the GSC were wrong by an arcsec or more. The same will happen during Cycle 1, but the frequency of failures will decrease as we improve the GSC and operational procedures.

The JWST data management subsystem has processed all commissioning and Cycle 1 observations to date, generating 1.5M files and requiring 55 TB to store a single copy. Users should be selective about which types of data products they download to avoid wasting network bandwidth and storage. Users can download and rerun the JWST calibration pipeline with custom parameters tailored to their needs. Users with good python skills can also modify or add steps to the calibration pipeline.

JWST data are now available in the MAST archive (see Accessing JWST Data). See Figure 30.

Early in Cycle 1, data products may have relatively poor calibration accuracy and contain calibration artifacts, because Cycle 1 observing began shortly after observatory commissioning, before instrument teams had finished generating new calibration reference files from the final commissioning observations. As instrument teams deliver improved calibration reference files, science operations will reprocess old data and make improved data products available in MAST.

Users should be especially vigilant about astrometric and photometric calibration errors in data products downloaded early in Cycle 1. Errors in guide star coordinates or focal plane geometry will propagate to the world coordinate system (WCS) for exposure-level data products. Higher-level products (e.g., mosaics) may use tweakreg and Gaia sources in each image to transform the WCS onto the Gaia frame. Photometric calibration will reflect pre-launch expectations until calibration reference data are updated.

Users should note the calibration pedigree of their data files and of data files used in publications. Consult JWST documentation for a description of known calibration issues and their resolution in successive versions of calibration reference data and software.

Data processing typically takes about a day, but can take longer if downlink, data transfer, or processing issues arise. For complicated modes (e.g., multi-object spectroscopy) or associations containing many exposures, the calibration pipeline can take several hours to run or even days in extreme cases. Performance will improve over time, but for now the main focus is functionality.

7.1 JWST User Documentation System (JDox) Updates

The JWST User Documentation system (JDox) provides comprehensive information about the JWST Proposing process, the Observatory and science instruments, science data characteristics and data access, data pipeline processing and calibration, as well as introductions to post pipeline data analysis tools and training materials. A new release of JDOX went live on July 12 2022. This release includes some 24 new articles, and flight updates to several dozen additional articles.

The new articles highlight such topics as data features and image artifacts seen in flight data, known shortcomings in current data pipeline products, and other articles to help users understand the status of the Observatory and science instruments. Updates to previous JDox articles include everything from minor fixes to preliminary commissioning information. A Breaking News page in the July 12 release provides guidance to the new and revised content as well as other important information for users.

Please note that many JDox updates will continue to appear from ongoing assessments of commissioning results and in-flight calibration data. At any time, users can refer to the Latest Update information box at the bottom of each article to see if and when that article has had significant updates made. JDox also maintains a summary page showing recently changed articles by titles and when they were updated.

STScI will republish JDox often over summer 2022 to disperse new information to the community as soon as it is available. Another major release will be made at the time of the Cycle 2 Call for Proposals, expected in November 2022.

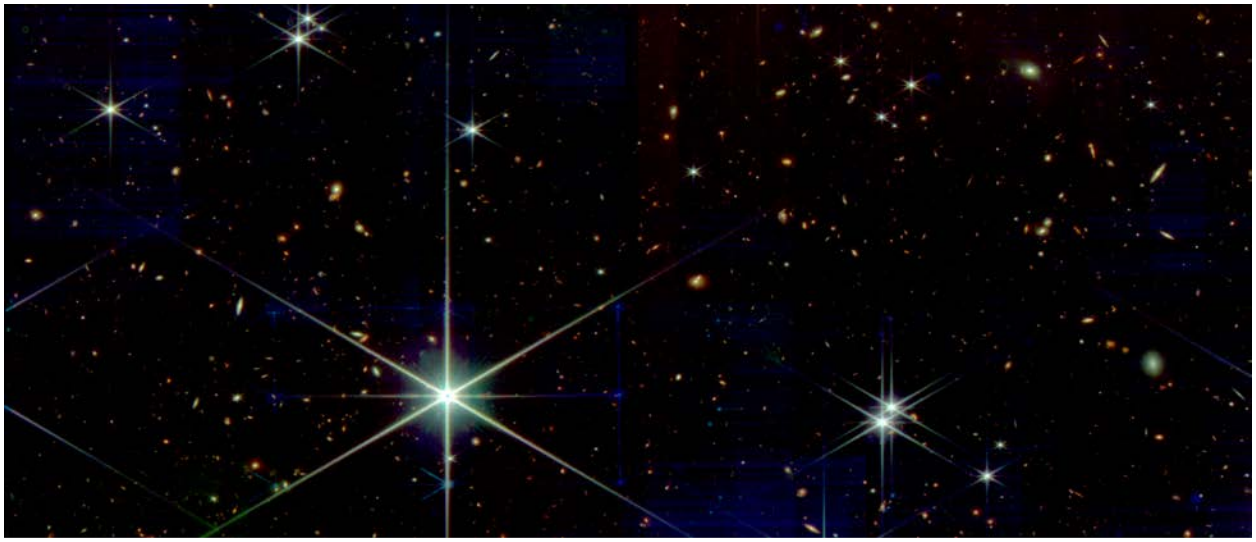

Figure 30: Multi-wavelength image mosaic of the Fine Phasing field, demonstrating the efficacy of automated data processing. *This is a color version of the image that was released just after the completion of telescope fine phasing; the blue, green and red channels show NIRCam F115W, F200W, and F356W. It was produced simply by retrieving the automatically-produced Level 3 mosaic data products from MAST, and opening them in ds9 to make an RGB image. The only manual step applied was a simple median subtraction of background level, used primarily to remove a temporarily-high background in the 3.5 μm channel in these early data, which appeared because the instruments were not yet fully cooled. The automated pipeline generates a nearly science-ready product with all mosaic tiles stitched and the several filters registered together. Data from PID 1160 observation 22. Several hundred spatially-resolved galaxies are present in this image.*

8.0 Closing thought

JWST is the product of the efforts of approximately 20,000 people in an international team. Commissioning JWST and characterizing science performance is the result of tremendous effort by the JWST commissioning team over the last six months. The achieved performance is the result of efforts over the many years leading to launch by team members across much of the globe. Given the measured performance described in this document, the JWST mission enters Cycle 1 having demonstrated that the observatory exceeds its demanding pre-launch performance expectations. With revolutionary capabilities, JWST has begun the first of many years of scientific discovery.